Nano Research

ISSN 1998-0124 CN 11-5974/O4
https://doi.org/10.26599/NR.2026.94909299

Research Article

Ternary Ag-Te-S colloidal quantum dots for shortwave infrared photodetectors

Zhixuan Wang[1,2], Ting Zhang[2], Zhiyong Tang[3], Ziyan Zhang[1,2], Yejun Zhang[2], Jiang Jiang[1,2], Tingfeng Yao[2](✉), Hongchao Yang[2](✉), Qiangbin Wang[1,2,3,4](✉)

[1] School of Nano-Tech and Nano-Bionics, University of Science and Technology of China, Hefei 230026, China

[2] CAS Key Laboratory of Nano-Bio Interface, Division of Nanobiomedicine and i-Lab, Suzhou Institute of Nano-Tech and Nano-Bionics, Chinese Academy of Sciences, Suzhou 215123, China

[3] School of Physical Science and Technology, ShanghaiTech University, Shanghai 201210, China

[4] College of Materials Sciences and Opto-Electronic Technology, University of Chinese Academy of Sciences, Beijing 100049, China

Nano Res., **Just Accepted Manuscript** • https://doi.org/10.26599/NR.2026.94909299

https://www.sciopen.com/journal/1998-0124 on Oct. 29, 2026

© The Authors(s)

Just Accepted

This is a "Just Accepted" manuscript, which has been examined by the peer-review process and has been accepted for publication. A "Just Accepted" manuscript is published online shortly after its acceptance,which is prior to technical editing and formatting and author proofing. Tsinghua University Press (TUP) provides "Just Accepted" as an optional and free service which allows authors to make their results available to the research community as soon as possible after acceptance. After a manuscript has been technically edited and formatted, and the page proofs have been corrected, it will be removed from the "Just Accepted" web site and published officially with volume and article number (e.g., *Nano Research*, **2025**, *18*, 94906990). Please note that technical editing may introduce minor changes to the manuscript text and/or graphics which may affect the content, and all legal disclaimers that apply to the journal pertain. In no event shall TUP be held responsible for errors or consequences arising from the use of any information contained in these "Just Accepted" manuscripts. To cite this anuscript please use its Digital Object Identifier (DOI®),which is identical for all formats of publication.

Just Accepted

TABLE OF CONTENTS (TOC)

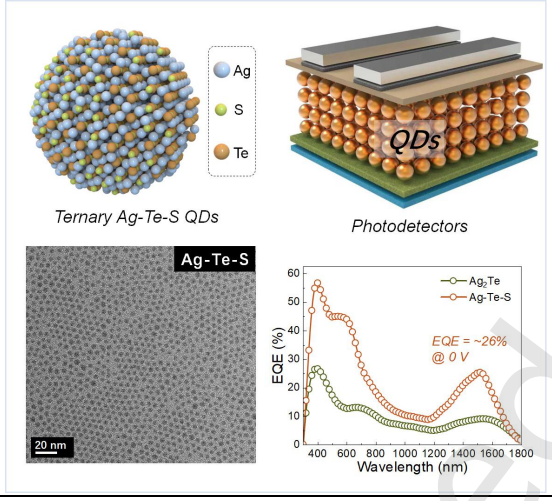

We have designed a ternary Ag-Te-S QDs with prolonged exciton dynamics, which have been employed in SWIR photodiodes, achieving an external quantum efficiency of 26% over 1.5 μm and a specific detectivity (D*) of 1.3×10^{11} Jones under 0 V bias at room temperature.

Just Accepted

Research Article

Ternary Ag-Te-S colloidal quantum dots for shortwave infrared photodetectors

Zhixuan Wang [1,2], Ting Zhang [2], Zhiyong Tang [3], Ziyan Zhang [1,2], Yejun Zhang [2], Jiang Jiang [1,2], Tingfeng Yao [2] ✉, Hongchao Yang [2] ✉, Qiangbin Wang [1,2,3,4] ✉

[1] School of Nano-Tech and Nano-Bionics, University of Science and Technology of China, Hefei 230026, China
[2] CAS Key Laboratory of Nano-Bio Interface, Division of Nanobiomedicine and i-Lab, Suzhou Institute of Nano-Tech and Nano-Bionics, Chinese Academy of Sciences, Suzhou 215123, China
[3] School of Physical Science and Technology, ShanghaiTech University, Shanghai 201210, China
[4] College of Materials Sciences and Opto-Electronic Technology, University of Chinese Academy of Sciences, Beijing 100049, China

Received: 28 October 2026; **Accepted: 29 October 2026**

✉Address correspondence to Tingfeng Yao, tfyao2022@sinano.ac.cn; Hongchao Yang, hcyang2014@sinano.ac.cn; Qiangbin Wang, qbwang2008@sinano.ac.cn

Cite this article: *Nano Research*, 2027, 20, 94909299 https://doi.org/10.26599/NR.2026.94909299

ABSTRACT: Ecofriendly silver telluride (Ag_2Te) colloidal quantum dots (QDs) are promising for shortwave infrared (SWIR) photodetectors. However, the performances of the devices–especially beyond 1.5 μm–remain constrained photoelectric conversion efficiency due to inefficient charge extraction. Here, we develop a ternary Ag-Te-S QDs via sulfur (S) pre-injection strategy. The incorporation of S atoms in Ag_2Te crystal lattice suppresses the particle fusion, improves structural uniformity, and prolongs the exciton dynamics. By integrating the ternary Ag-Te-S QDs into SWIR photodiodes, the devices achieve a state-of-the-art external quantum efficiency (EQE) of 26% beyond 1.5 μm under 0 V bias at room temperature. We finally demonstrate SWIR fluorescence imaging by using the Ag-Te-S QD photodiodes. This work establishes a practical polynary alloy design to overcome charge-extraction bottlenecks in colloidal QD photoactive layers for eco-friendly high-performance SWIR photodetection.

KEYWORDS: Short-wave infrared, ternary quantum dots, photodiodes, exciton dynamics

1 Introduction

Colloidal quantum dots (QDs)-based shortwave infrared (SWIR) photodetectors have attracted increasing attention due to their solution-processability, size-tunable bandgap, and compatibility with low-cost fabrication techniques[1]. Recently, Ag_2Te QDs are considered promising candidates for SWIR photodetection owing to their intrinsic infrared absorption and favorable optoelectronic properties[2–6]. Considerable efforts have been devoted to improving the device performances of Ag_2Te QD photodetectors. Key advances include the development of suitable tellurium precursor systems, which enable simple manipulation of the precursor ratio to control the size of the Ag_2Te QDs and improve photon absorption efficiency in the desired wavelength range, thereby enhancing the detector's response to target infrared signals[7]. Additionally, efforts to passivate QD surface defects and improve charge transport at the interfaces, while suppressing recombination at the interfaces, have laid a solid foundation for the continued development of Ag_2Te QD photodetectors[8–11].

However, the performances of SWIR Ag_2Te QD photodetectors, especially external quantum efficiency (EQE) at detected peak wavelength, is still unsatisfactory. For QD photodetectors, efficient transport of photogenerated carriers within the active layer not only depends on light absorption and interfacial charge transfer, but also critically affected by charge separation within individual QDs and charge transport between neighboring QDs. Thus, the exciton dynamics of QDs also plays a central role in determining photodetector performances by influencing the carrier separation, transport, and extraction[12–14]. For instance, QDs with a short excited-state lifetime generally means that the photogenerated carriers tend to undergo rapid recombination before interfacial migration and extraction, which is unfavorable for efficient charge separation and collection in devices[15–18]. Therefore, regulating the intrinsic excited-state lifetime of QDs are important directions for further improving SWIR photodetection performance[19]. To address these issues, previous studies have attempted to tailor the Ag_2Te QDs by surface engineering such as ligand chemistry and halide ions passivation[11,20–22]. Nevertheless, the intrinsic issues of inorganic core of Ag_2Te QDs have not yet been resolved.

Here, we report a sulfur pre-injection strategy to construct a ternary Ag-Te-S QDs. The sulfur incorporation modifies the local chemical environment within the ternary QDs, which prolongs the effective excited-state lifetime, thereby facilitating carrier separation inside the QDs and carrier transfer toward the surface. Based on the optimized Ag-Te-S QDs, the resulting *p-i-n* photodiodes deliver an external quantum efficiency (EQE) of 26% at $\lambda > 1.5$ μm, corresponding to a room-temperature specific detectivity (D^*) of 1.3×10^{11} Jones. Finally, we

Just Accepted

successfully demonstrated the SWIR imaging by using the detectors.

2. Experimental

2.1. Chemicals

Silver acetate anhydrous (AgAc, 99%) were purchased from Alfa Aesar. 1-Dodecanethiol (DT, ≥98%) and 3-mercaptopropionic acid (MPA; 99%) from Thermo fisher. Triphenyl phosphate (TPP, ≥98%), Sulfur powder (S, ≥99.99%), Dodecane (≥99%, GC), ethyl acetate (EA, AR grade), and tellurium oxide (TeO_2, 99.999%) were purchased from Aladdin. Methanol (99.5%), anhydrous ethanol (99.7%), and chloroform were purchased from Sinopharm Chemical Reagent Company. All these reagents were of analytical grade and used without further purification.

2.2 Synthesis of Ag_2Te QDs

The tellurium precursor was prepared by dissolving 1.25 mmol TeO_2 in 5 mL DT under heating at 100 °C within a nitrogen environment (0.25 M TeO_2-DT). In a separate 100 mL three-necked flask, 1 mmol AgAc was combined with 5 mL dodecane and 10 mL DT. This mixture underwent continuous stirring while being heated to 110 °C under a continuous flow of high-purity nitrogen gas, followed by gradual temperature elevation to 160 °C. During this thermal process, the mixture transitioned to a yellow transparent solution. Then, 1.6 mL 0.25 M TeO_2-DT precursor solution was rapidly introduced into the reaction vessel, triggering an instantaneous color transformation to dark black. Following 5 minutes of reaction maintenance, the system underwent natural cooling after heat termination. Subsequent purification involved sequential washing with chloroform and methanol through centrifugal separation.

2.3 Synthesis of Ag-Te-S QDs

In a separate 100 mL three-necked flask, 1 mmol AgAc was combined with 5 mL dodecane and 10 mL DT. This mixture underwent continuous stirring while being heated to 110 °C under a continuous flow of high-purity nitrogen gas, followed by gradual temperature elevation to 160 °C. During this thermal process, the mixture transitioned to a yellow transparent solution. Then, 0.3 mL S-TPP precursor (0.5 M, S powder was dissolved in TPP) was rapidly introduced into the reaction vessel, and subsequently 1.1 mL TeO_2-DT was added in 30 s. Following 5 minutes of reaction maintenance, the system underwent natural cooling after heat termination. Subsequent purification involved sequential washing with chloroform and methanol through centrifugal separation.

2.4 Material characterization

The morphologies of QDs were examined through a Tecnai G2 F20 S-Twin transmission electron microscopy (TEM) at an acceleration of 200 kV. Powder X-ray diffraction (PXRD) patterns were recorded on a Bruker D8 Advance powder X-ray diffractometer, using Cu-Kα radiation (λ = 1.54056 Å). The absorption spectra were recorded with UV-3600 Plus ultraviolet–visible–near infrared ray (UV-vis-NIR) spectrophotometer (SHIMADZU, JAPAN). The emission spectra were measured using a near-infrared spectrometer (NIR17S, Ideaoptics) with an 808 nm laser as the excitation source. XPS data were collected under ultrahigh vacuum (10^{-8}~10^{-9} Torr) by an ESCALAB 250 XI system with a monochromatic X-ray source (Al Kα source, UPS data were obtained on an electron spectrometer using monochromatic HeI radiation at 21.22 eV). High-resolution XPS data were collected from the regions around Ag 3d, Te 3d and S 2p. The surface morphology of the QD films was characterized by field-emission scanning electron microscopy (SEM, Regulus8230, Hitachi). The samples were spin-coated onto 1×1 cm^2 ITO substrates for testing. PLQY and time-resolved PL spectra were tested with FLS1000.

2.5 Transient absorption spectroscopy measurement

Transient absorption (TA) measurements were performed on a Yb:KGW regenerative amplified femtosecond laser system (Light Conversion, 800 nm, 200 fs, 42 μJ/cm^2 and 100 kHz repetition rate) and a Femto-TA100 spectrometer (Time-Tech Spectra LLC.). The lasre fundamental output was split in two parts with a 90:10 beam splitter. The 90% parts was used to pump an Orpheus-HP optical parametric amplifier (Light Conversion) to generate a wavelength-tunable pulse as the pump beam. The remaining 10% portion was further attenuated and focus onto a 3-mm-thick YAG crystal to generate a probe beam covering the wavelength range of 1000-1650 nm. The pump beam was chopped by a mechanical chopper at 4165 Hz, and the change in absorbance with and without the absence of pump beam was calculated with the intensity of the adjacent 12 probe pulses. The diameter on the sample for pump and probe spots was about 440 μm and 125 μm, respectively. The typical instrument response is well fitted by a Gaussian function with ~200 fs FWHM.

The QD-TCA-Rub solution was sealed in a 2 mm cuvette with N_2 environment and was under continuous stirring during measurements. All experiments were performed under room temperature. The data was analyzed through commercial software (Surface Xplorer, Ultrafast Systems).

2.6 Device fabrication

The glass substrates with a patterned ITO anodes were cleaned sequentially in ultrasonic baths of ethanol, acetone, and isopropanol for 15 min each; and then, the cleaned ITO was subjected to a UV-ozone treatment for 30 min. Subsequently, SnO_2 NPs were spin-coated on the ITO glass at 3000 rpm for 45 s, and finally, annealing at 150 °C for 30 min in ambient air. Three layers of QDs were further deposited on top of SnO_2 films. For each QD layer, 40 mg mL^{-1} QD solution was spin coated at 3000 rpm for 30 s and ligand-exchanged with MPA/EA (0.5 vol%) for 30 s, followed by rinsing twice with EA. P3HT layers were spin-coated at 3000 rpm for 45 s using an 8 mg/mL chlorobenzene solution. Under vacuum (<1×10^{-6} torr), the top electrode layers, consisting of 10 nm of MoO_3 and 100 nm of Ag, were successively deposited onto the ITO/SnO_2/QD/P3HT structure by a thermal evaporator at a rate of 0.1 and 1 Å s^{-1}, respectively.

2.7 Device characterization

The J-V characteristics of photodetector was measured on a semiconductor analyzer (Keithley 4200A-SCS). The noise spectral density was measured using a low frequency noise test

Just Accepted

system (LFN-2000) in RMS average mode. The system comprises a low-noise current amplifier (DHPCA-300, Femto) and a DAQ (NI 6341), with an extremely low noise background of 10^{-16} A/Hz$^{0.5}$. Broadband EQE measurements were performed on the QE-R measurement system (Enlitech), with the Xenon intensity calibrated using standard Si detector and InGaAs detector. The time response of the device was measured using an oscilloscope (Keysight DSOX1204A) and a transimpedance amplifier (Stanford SR570). A 532 nm lase modulating 1 kHz by a waveform generator (Keysight 33500B) was used as a light source. The TPC decay was measured under 0 V with a 532 nm laser and the pulse width was set to 8 μs and frequency to 20 kHz. Mott-Schottky analysis was conducted based on the measurement of the capacitance-voltage curve. The equipment used was a multichannel potentiometer (VMP300, Biologic), with the test frequency set at 50 kHz, a voltage range of −0.5 to 0.8 V, a step size of 40 mV, and an amplitude of 20 mV. All the device characterizations were performed in air under ambient conditions.

3. Result and Discussions

3.1 Synthesis and Characterization of Ternary Ag-Te-S QDs

The preparation of ternary Ag-Te-S QDs was developed by a modified conventional hot-injection method. In their typical synthesis (**Figure S1**), sulfur precursor was first injected in Ag-precursor solution, followed by addition of tellurium precursor to form Ag-Te-S QDs. Owing to the high reactivity between S and Ag, the S pre-injection rapidly generates small Ag_2S intermediates. Their formation alters the local Ag/S reaction environment prior to Te addition and thereby influences the subsequent formation of the Ag-Te-S QDs. As shown in **Figure 1a**, the transmission electron microscopy (TEM) image manifests Ag-Te-S QDs consist predominantly of spherical or quasi-spherical particles with particle size of 4 nm (**Figure S2**), while in **Figure S3**, the Ag_2Te QDs exhibit a substantial fraction of rod-like or ellipsoidal particles, together with pronounced particle fusion[26]. This behavior is associated with the large ion radii of Te^{2-} leading to polarization. The rod-like structure or orientated growth tendency have also observed in other metal telluride nanocrystals, such as CdTe[27] and HgTe[28]. This S pre-injection nuclei and Te post-introduction method to form Ag-Te-S QDs suppress the QDs fusion and anisotropy morphology. The high-resolution TEM (HRTEM) images display the lattice fringes of facet (122) for Ag_2Te with a lattice spacing of 2.46 Å, while in Ag-Te-S, the lattice fringes with a smaller spacing of 2.41 Å. Energy-dispersive X-ray spectroscopy (EDS) mappings of the Ag-Te-S QDs (**Figure 1b**) present the homogeneous distribution of Ag, Te, and S elements in the whole nanoparticle, and the powder X-ray diffraction (XRD) patterns reveal no another impurity peaks (**Figure 1c**). Moreover, the main diffraction peak at ~42° for Ag-Te-S QDs shifts to higher angles relative to that of Ag_2Te. This observation is consistent with lattice contraction induced by smaller- radius S ions, which reduces the interplanar spacing *d*. According to Bragg's law, such lattice contraction leads to the higher- angle shift of X- ray diffraction peaks. This result agrees with the HRTEM of decreased lattice spacing and suggests the S incorporation in Ag_2Te QDs. Then, the X-ray photoelectron spectroscopy (XPS) was further employed to examine the overall evolution of the chemical states after sulfur incorporation. **Figure 1d** shows the high-resolution Ag 3d region. Compared with Ag_2Te QDs, the Ag $3d_{3/2}$ and Ag $3d_{5/2}$ peaks of the Ag-Te-S QDs give a positive shift of ~0.1 eV, and the similar shift are also observed in Te $3d_{3/2}$ and Te $3d_{5/2}$ peaks (**Figure S4**). These indicate that the local chemical environments of both Ag and Te were altered after S incorporation, making the outer-shell electrons of the corresponding lattice atoms more difficult to ionize. Considering that sulfur has a higher electronegativity (2.6) than both Ag (1.9) and Te (2.1), the introduction of S can reduce the electron density around Ag and Te atoms, thereby increasing their binding energies. **Figure 1e** shows the high-resolution S 2p spectra. According to the peak deconvolution results, the Ag-Te-S QDs exhibited an additional sulfur signal attributable to lattice S atoms within the QDs[29], whereas the sulfur signal in the Ag_2Te QDs originated only from the thiol ligands. At the same time, the binding energies of ligand-bound S in the Ag-Te-S QDs were slightly higher than those of ligand S on the surface of the Ag_2Te QDs (approximately 162.76 and 161.60 eV, respectively), agreeing with the Ag 3d and Te 3d regions. These results demonstrate that S element was successfully introduced into the Ag_2Te system to form ternary Ag-Te-S QDs. Furthermore, to determine the S content in Ag-Te-S QDs, we employed inductively coupled plasma mass spectrometry (ICP-MS) and thermogravimetric analysis (TGA), as shown in **Figure S5** and **Table S1**. **Figure 1f** depicts the element ratios from ICP-MS and TGA data, in which the Ag/Te ratio raised from 2.08 to 2.75 and the total S/Te ratio increased from 0.56 (for Ag_2Te) to 0.97 (for S-containing Ag_2Te-based QDs with lattice Te/S ratio of 0.73/0.27). The trends in both S/Te and Ag/Te ratios consistently indicate an increased sulfur fraction in the Ag-Te-S QDs, providing further evidence for the successful incorporation of S atoms.

Subsequently, we investigated the optical properties of the QDs. As shown in **Figure 1g**, the Ag-Te-S QDs exhibit a pronounced excitonic absorption feature centred at ~1300 nm with a peak-to-valley ratio of approximately 1.2, accompanied by a 50-nm blue shift to shorter wavelengths (vs. Ag_2Te QDs) owing to the S incorporation leading bandgap increase. The PL spectra (**Figure 1h**) show Ag-Te-S QDs with lower intensity with PL quantum yield (PLQY) of 0.12% (0.79% for Ag_2Te, **Figure S6**). Time-resolved PL spectra in **Figure 1i** present the Ag-Te-S QDs have short average PL lifetime (τ_{avg}, **Table S2**), consistent with these PL data. To further probe the S effect in Ag-Te-S QDs, a control sample was prepared by injecting only the sulfur precursor (forming Ag_2S QDs) with the same amount used in Ag-Te-S QDs. As depicted in **Figure S7**, the Ag_2S QDs exhibits a photoluminescence (PL) emission peak at ~1000 nm, while no Ag_2S-related emission in the Ag-Te-S QDs was observed in 900-1200 nm range. Instead, the Ag-Te-S QDs displayed a single emission band over the range of 1400 nm. The absorption[30] and PL behavior markedly differs from the dual-emission characteristics of a simple physical mixture of independent Ag_2S and Ag_2Te QDs (Figure S7d). These results indicate that, in our synthetic system, the S and Te precursors did not independently nucleate into two isolated QD populations to produce physical mixture, but form S containing Ag_2Te-based QDs.

Under Review

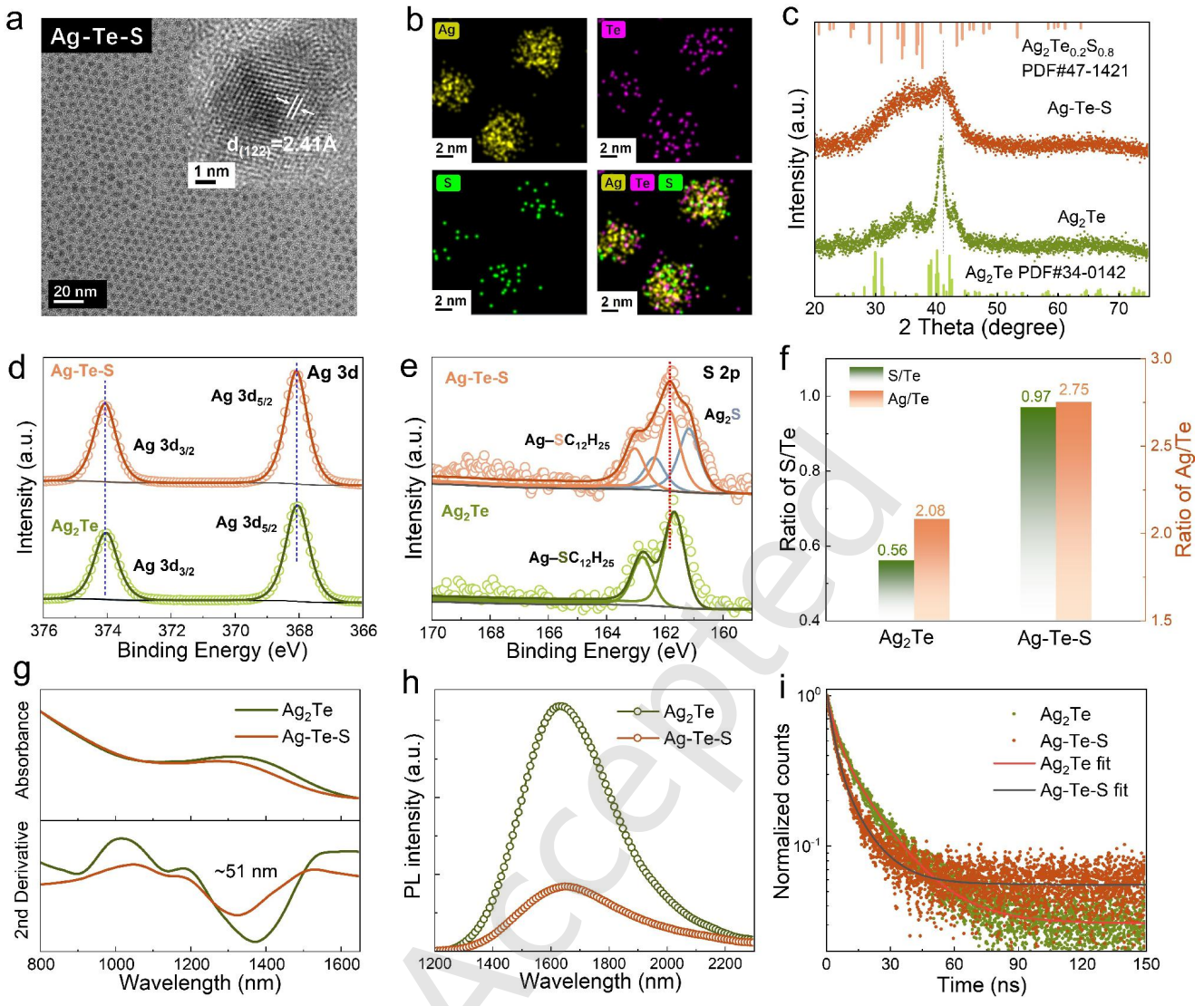

Figure 1. (a) TEM and HRTEM images of Ag-Te-S QDs. (b) EDS elemental maps of Ag-Te-S QDs. (c) Powder XRD patterns of Ag_2Te and Ag-Te-S QDs. High-resolution XPS spectra of Ag 3d (d) and S 2p (e) of Ag_2Te and Ag-Te-S QDs. (f) The ratio of S/Te and Ag/Te in two groups of Ag_2Te and Ag-Te-S QDs. (g) Absorption spectra of Ag_2Te and Ag-Te-S QDs and their second derivatives. (h) Room temperature steady-state PL (h) and time-resolved PL (i) spectra of Ag_2Te and Ag-Te-S QDs.

3.2 Exciton Dynamics of Ag-Te-S QDs

Then, we evaluated the potential of Ag-Te-S QDs in optoelectronic devices by investigating the exciton dynamics of the Ag_2Te and Ag-Te-S QDs via transient absorption (TA) spectroscopy. The absorption spectra in tetrachloroethylene (TCE) are shown in **Figure S8**. TA spectra were collected from 1100 to 1700 nm; strong negative signals at 1468 nm for Ag_2Te and 1401 nm for Ag-Te-S arise from ground-state bleaching (GSB, **Figure 2a, b** and **Figure S9**). To more clearly compare the exciton decay behaviors of the two materials, kinetic traces were extracted at their respective bleach maxima and fitted accordingly. As shown in **Figure 2c**, the decay dynamics of both samples could be well fitted to a tri-exponential decay with the following function: $\Delta A = A_1 \cdot \exp(-\tau/\tau_1) + A_2 \cdot \exp(-\tau/\tau_2) + A_3 \cdot \exp(-\tau/\tau_3) + B$, where A_i and τ_i (i = 1, 2, 3) are the amplitudes and corresponding decay times, respectively. The fitted parameters are presented in **Table S3**, in which the fast-decay components are mainly associated with nonradiative recombination or trap-assisted carrier capture processes occurring on the timescale of tens of picoseconds, and long-decay components belong to exciton recombination (>2 ns)[28]. According to the fitted parameters, after sulfur incorporation, the contributions of the fast components to the total TA signal decrease from 0.39 to 0.28 (for absolute A_1), and 0.23 to 0.10 (for absolute A_2), respectively. Correspondingly, the contribution of the long decay component (A_3) increases from 0.30 for Ag_2Te to 0.53 for Ag-Te-S QDs, indicating an increased proportion of long-lived excitonic processes. Compared with Ag_2Te QDs, which exhibited an average exciton lifetime of 2.12 ns, the Ag-Te-S QDs showed a longer average exciton lifetime of 3.30 ns, which is expected to facilitate carrier extraction and collection in devices and thus leads to enhanced performance[31–34]. The suppressed fast nonradiative recombination likely originates from sulfur incorporation into the anionic sublattice to form ternary QDs, which modulates their local electronic and energy-level structures, and prolongs the excited- state lifetime, thereby conducive to facilitating charge extraction and suppressing recombination- related current.

UPS measurements further showed that the energy-level structures of the two QD films with Fermi levels of 4.42 eV for Ag_2Te and 4.49 eV for Ag-Te-S (**Figure S10**). This small

Just Accepted

difference suggests that the improved device performance is unlikely to mainly arise from a substantial shift in the energy-level structure. These combined improvements are expected to promote more efficient transport and collection of photogenerated carriers in the QD active layer, thereby providing a favorable material basis for constructing high-performance SWIR photodetectors. We next evaluated the morphology and charge-transport properties of the QD films. As shown by the SEM images in **Figure S11**, the Ag_2Te QD film contained a considerable number of pinholes, whereas the Ag-Te-S film exhibited a more uniform and smoother morphology. Such an improved film morphology is beneficial for reducing local leakage pathways and defect trapping sites, thereby suppressing nonradiative carrier loss within the film and enhancing interdot charge transport.

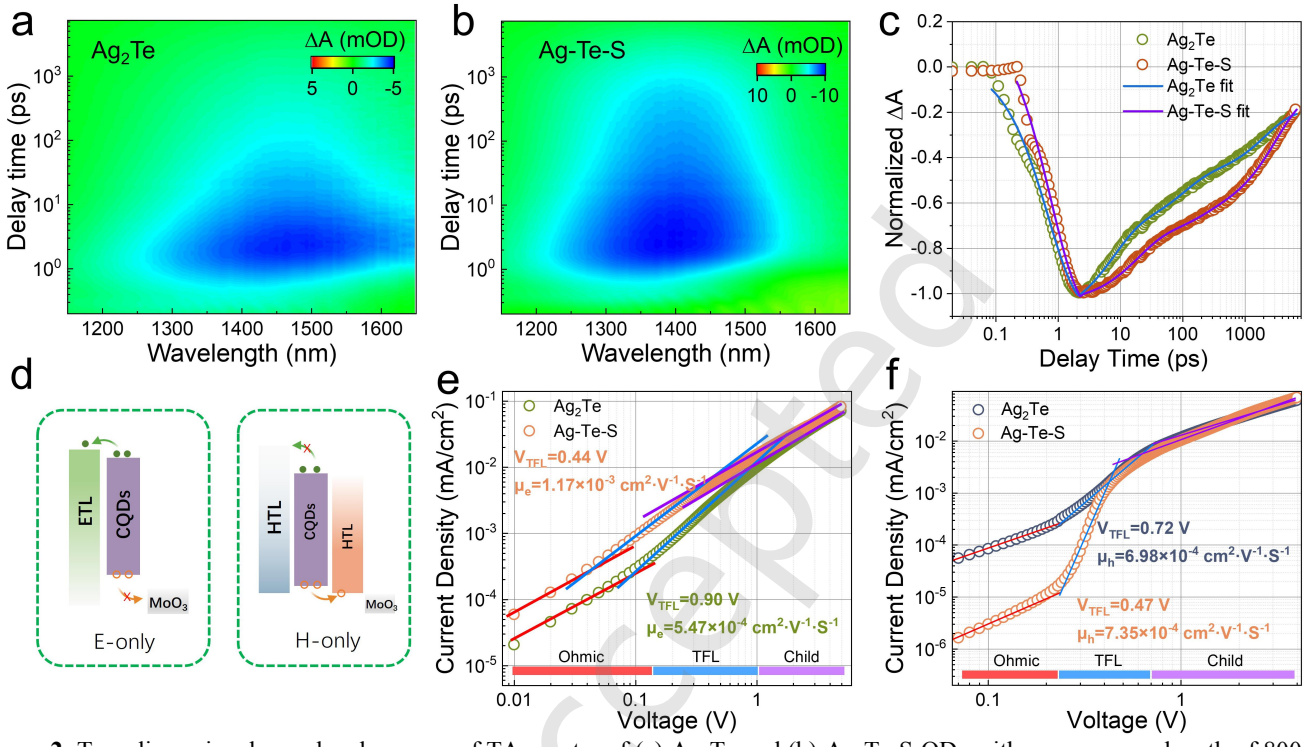

Figure 2. Two-dimensional pseudocolour map of TA spectra of (a) Ag_2Te and (b) Ag-Te-S QDs with a pump wavelength of 800 nm. (c) Kinetic trace at a probe of Ag_2Te (1468 nm) and Ag-Te-S QDs (1401 nm). (d) Schematic illustration of the electron-only and hole-only devices. *J-V* curves of the (e) electron-only devices and (f) hole-only devices using the SCLC technique.

To quantitatively evaluate the defect states and carrier mobilities of the films, single-carrier devices were further fabricated and analyzed using the space-charge-limited current (SCLC) technique (**Figure 2d-f**). Typically, an SCLC curve can be divided into three regions according to the change in slope: the Ohmic region, the trap-filled limit (TFL) region, and the trap-free SCLC (Child) region. At relatively low voltages, the TFL region is more strongly influenced by trap states in the film. The corresponding transition voltage, V_{TFL}, represents the voltage required for carriers to fill the traps and can be used to estimate the trap-state density, N_t [35]. For electron-only devices (Figure 2d), the Ag-Te-S film exhibited a smaller V_{TFL} value (0.44 V) than that of Ag_2Te film (0.90 V). The hole-only devices also reveal the similar variation tendency of V_{TFL} (Figure 2f), indicating a significantly reduced trap-state density for both electron and hole in Ag-Te-S QD films (**Table S4**)[36]. As the applied voltage increased further, the slope of the *J-V* curve changed again and entered the Child region. The carrier mobility (μ) of the film can then be calculated from the voltage and current density at the transition between the TFL and Child regions[35]. The SCLC data revealed that, both the electron mobility (1.17×10^{-3} $cm^2\cdot V^{-1}\cdot s^{-1}$) and hole mobility ($7.35\times10^{-4}$ $cm^2\cdot V^{-1}\cdot s^{-1}$) of the Ag-Te-S film were higher than those of the Ag_2Te film, with the improvement in electron mobility being more pronounced. These results indicate that sulfur incorporation not only improves the film morphology, but also optimizes the charge-transport pathways within the film, enabling more efficient electron transport between neighboring QDs.

3.3 Ag-Te-S QDs SWIR Photodetectors

We then integrate the ternary Ag-Te-S QDs into photodiodes. The device structure follows a typical *p-i-n* architecture of ITO/SnO_2/QDs/P3HT/MoO_3/Al[6] (**Figure 3a**). The QD active layers underwent solid-state ligand exchange with MPA to improve charge transport. In **Figure 3b**, cross-sectional SEM image clearly resolves each functional layer and the Ag-Te-S QD active layer with ~113.3 nm thick (~132.2 nm for Ag_2Te QD device, **Figure S12**) and good interfacial contact with adjacent layers. Current density-voltage (J-V) characteristics are shown in **Figure 3c**. The Ag-Te-S QD devices give a dark current density of ~6×10^{-6} A/cm^2 under -0.1 V bias, lower than that of the Ag_2Te QD device (~7×10^{-6} A/cm^2 under -0.1 V bias). Under same illumination, the Ag-Te-S QD devices exhibit a higher current density. This result indicates that sulfur incorporation in ternary Ag-Te-S QDs enables the device to achieve an effectively suppressed dark current. To further evaluate the charge-separation capability within the device, Mott–Schottky analysis was performed[28]. **Figure 3d** exhibits the Ag-Te-S device exhibited a higher built-in potential than the control device (0.41 V vs. 0.23 V). This is consistent with the foregoing material and film characterizations and also helps explain the pronounced increase in dark current under reverse bias in the control Ag_2Te device, where the rapid carrier

Just Accepted

nonradiative recombination leads to a weaker built-in field and insufficient suppression of reverse current. The external quantum efficiency (EQE) and responsivity are shown in **Figure 3e** and **Figure S13**. The Ag-Te-S devices exhibit significantly improved photoelectric conversion efficiency over a broad spectral range. At the peak near 1520 nm under zero bias, the EQE reached ~26% for Ag-Te-S devices, compared with ~10% for Ag_2Te QD devices, with corresponding peak responsivities of ~0.34 and 0.12 A/W, respectively. This enhancement was further validated by statistical analysis of the net photocurrent at 0 V and the peak EQE collected from over 25 photodiodes, confirming the robustness and reproducibility of the performance enhancement (**Figure S14**). **Figure S15** and **S16** present active-layer-thickness-dependent absorption and EQE for both Ag_2Te and Ag-Te-S devices, which demonstrating an optimum QD thickness at approximately three deposited layers. The absorptance measurements on the completed photodiode device with three-layer Ag-Te-S QDs yield a peak absorptance of 60% (**Figure S17**), exceeding their peak EQE of ~26%. This discrepancy aligns with the photophysical behavior and validates the device architecture. The bias-dependent EQE measurements have been performed for both devices (**Figure S18**). Upon applying reverse bias, the carrier- collection efficiency is moderately improved, leading to a slight enhancement of EQE.

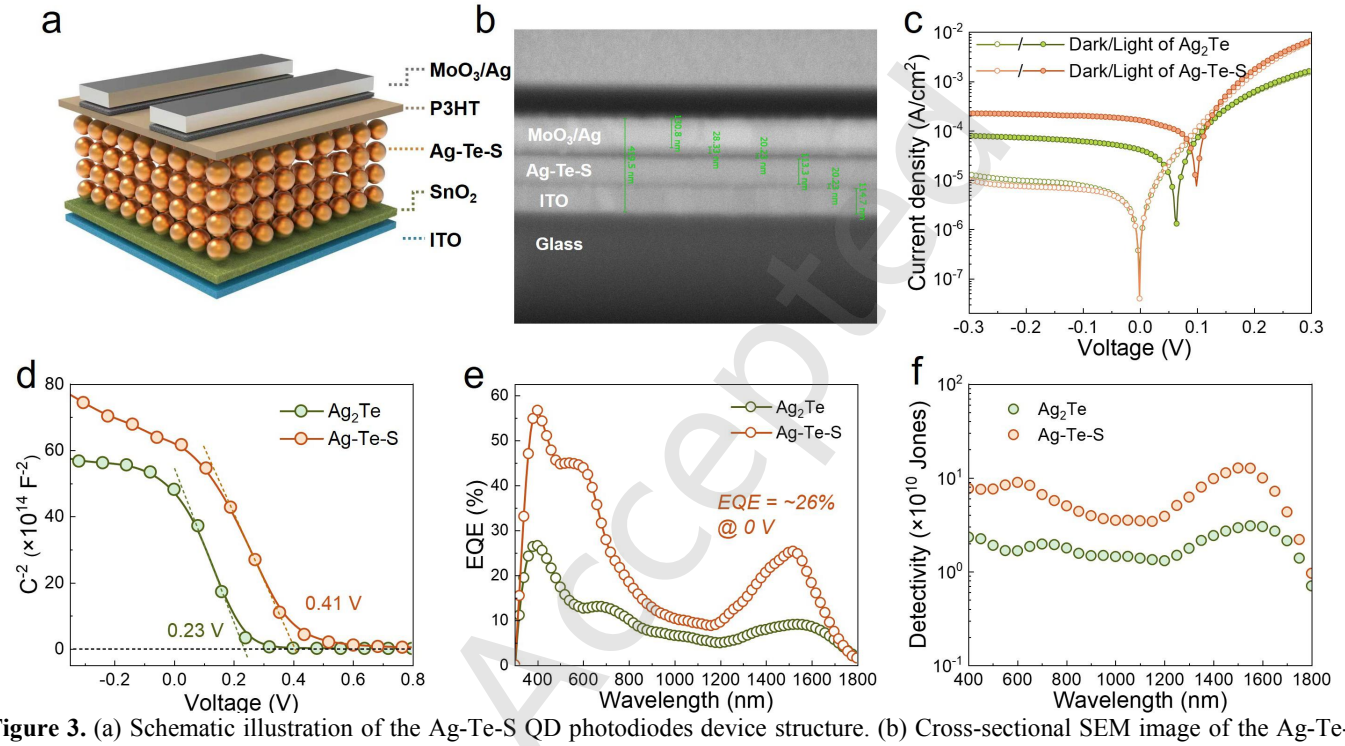

Figure 3. (a) Schematic illustration of the Ag-Te-S QD photodiodes device structure. (b) Cross-sectional SEM image of the Ag-Te-S QD photodiode. (c) Dark and illuminated current density–voltage characteristics of Ag_2Te and Ag-Te-S QD photodiodes measured under 1532 nm illumination with a power density of 0.5 mW cm^{-2}. (d) Capacitance-voltage characteristics of Ag_2Te and Ag-Te-S QDs photodiodes. (e) Broadband external quantum efficiency (EQE) spectra of Ag_2Te and Ag-Te-S QD photodiodes. (f) Broadband Specific detectivity spectra of Ag_2Te and Ag-Te-S QD photodiodes.

The specific detectivity (D^*) was calculated using the following formula[37]: $D^* = R \times (A \times \Delta f)^{1/2}/i_n$, where R is responsivity, i_n is noise current (at 1 Hz), A is device area (0.06 cm^2), and Δf is electrical bandwidth (1 Hz). As shown in **Figure S19**, the noise current of the Ag-Te-S device exhibited a noise current of 5.8×10^{-13} A/$Hz^{0.5}$ at 1 Hz and 0 V. For comparison, the shot-noise and thermal-noise limits were calculated as $i_{shot} = (2qI_d)^{1/2}$ and $i_{thermal} = (4kT/R)^{1/2}$, respectively. At 0 V, the corresponding values are 8.02×10^{-14} and 1.8×10^{-13} A $Hz^{-1/2}$. The measured noise remains higher than both calculated fundamental limits, while the instrumental background is substantially lower. Then, corresponding D^* is calculated of 1.3×10^{11} Jones (**Figure 3f**). We have also included a quantitative comparison of some key metrics, including detection wavelength (λ), external quantum efficiency (EQE), responsivity (R), specific detectivity (D*) among our Ag-Te-S QD photodetector and representative QD and commercial InGaAs photodiodes, as summarized in **Table S5, S6**. Commercial InGaAs photodiodes, as mature and systematically optimized devices, exhibit prominent performance advantages. We primarily demonstrate the potential of eco- friendly Ag-Te-S QDs for SWIR photodetector application. Compared to recently developed counterparts, the Ag-Te-S QDs reveal notable performance advancement. The linear dynamic range (LDR) exceeded 90 dB (**Figure S20**), demonstrating excellent performance across a broad illumination range. Meanwhile, the Ag-Te-S devices still maintained response times in the microsecond regime, with τ_{rise} = 24.2 μs and τ_{fall} = 48.1 μs (**Figure S21**). The frequency-dependent response was measured at 0 V bias, and the Ag-Te-S devices exhibits a bandwidth of 29.1 kHz (**Figure S22**). In addition, the optimized devices were subjected to continuous photoresponse testing under ambient air conditions without encapsulation. As shown in **Figure S23**, the devices still maintained good photoresponse capability after more than 60 h, indicating that the Ag-Te-S QD devices possess good stability.

Just Accepted

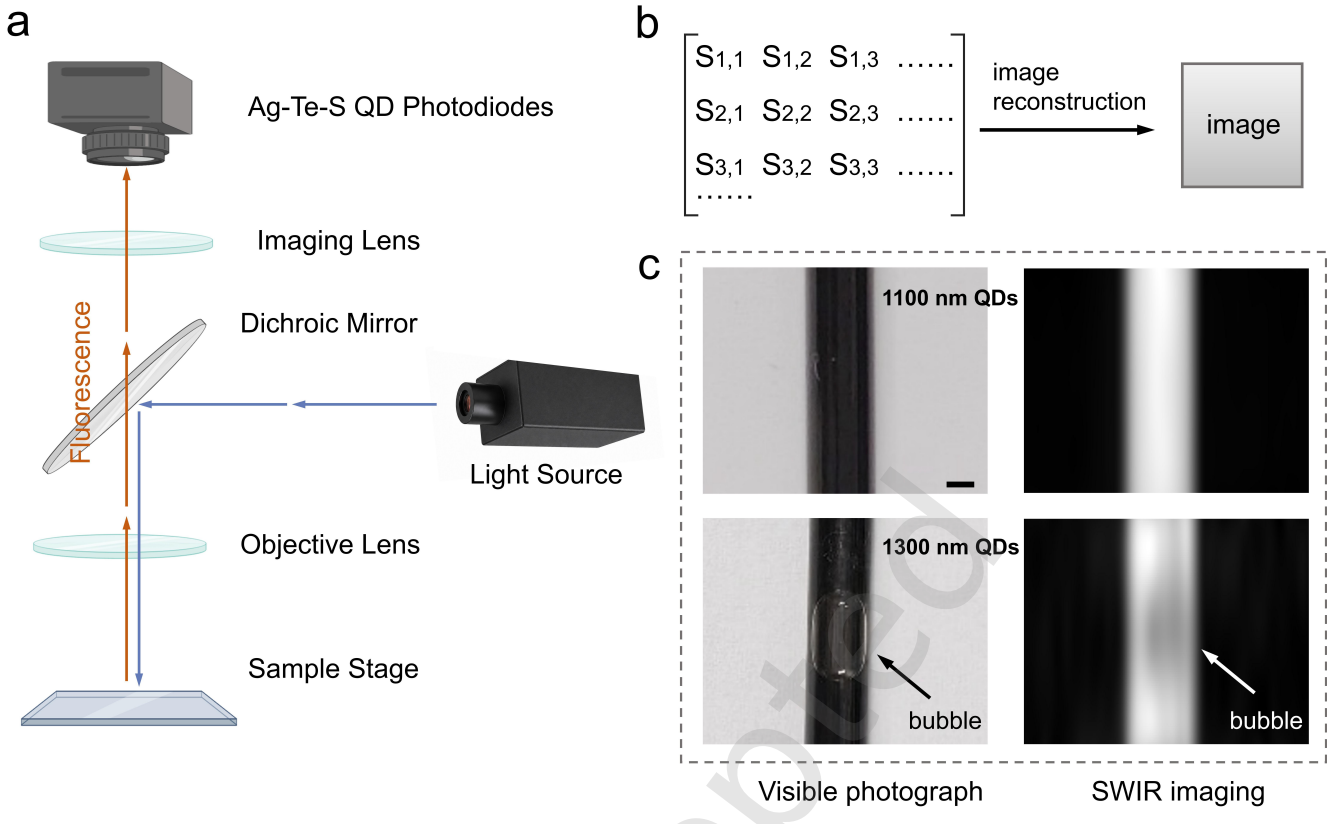

Figure 4. (a) Schematic of the SWIR imaging system utilizing Ag-Te-S QD photodetectors. (b) Data processing of the SWIR imaging system. (c) Visible and SWIR images of the QDs solutions in tube, scale bar: 2 mm. The visible-light photograph acquired under white-light illumination using camera, while the SWIR image acquired using SWIR camera under 808 nm laser.

We finally demonstrate the SWIR imaging characteristics of the Ag-Te-S QD photodiodes by testing the fluorescence signal of SWIR fluorophores. As depicted in **Figure 4a**, the imaging system consists of four main components, Ag-Te-S QD detector, lens, dichroic mirror, and light source. The 808 nm laser served as the light source and the infrared images were built on a data point array (**Figure 4b**). And we used the imaging system to detect the fluorescence signal of self-synthesized nanoprobes (AgAuSe QDs with emission center at 1100 nm and Ag_2Se QDs emitted at 1300 nm). As shown in **Figure 4c**, the fluorescence signal of QDs was clearly captured by the imaging system.

4. Conclusion

In summary, we developed a sulfur pre-injection strategy to synthesize Ag-Te-S ternary QDs through a modified hot-injection process. This approach effectively regulates the local chemical environment and nucleation/growth kinetics of the Ag-Te system, yielding QDs with improved structural uniformity, reduced defect density, and prolonged exciton lifetime. These materials also exhibit improved film morphology and charge-transport properties, which together promote more efficient photogenerated carrier extraction and collection. As a result, the corresponding photodiodes exhibit a substantially enhanced photoresponse, achieving an EQE of 26% at 1520 nm under zero bias, together with a peak specific detectivity of 1.3×10^{11} Jones. We finally demonstrated the SWIR fluorescence imaging by using the Ag-Te-S QD photodiodes. This work establishes a practical composition design to overcome charge-extraction bottlenecks in colloidal SWIR QD photodetection and demonstrate the application potential of the ecofriendly QDs photodetectors for of SWIR imaging.

Electronic Supplementary Material: Supplementary material (Figures S1–S23 and Tables S1–S6) is available in the online version of this article at https://doi.org/10.26599/NR.2026.94909299.

Data availability

All data needed to support the conclusions in the paper are presented in the manuscript and/or the Electronic Supplementary Material. Additional data related to this paper may be requested from the corresponding author upon request.

Acknowledgments

This work was financially supported by the National Key Research and Development Program of China (Grant Nos. 2024YFA1803402), the National Natural Science Foundation of China (Grant Nos. 22271308, 22127808), the Basic Research Program of Jiangsu Province (Grant Nos. BK20240124). The authors are grateful for the technical support from the Vacuum Interconnected Nanotech Workstation (Nano-X) of Suzhou Institute of Nano-Tech and Nano-Bionics, Chinese Academy of Sciences (SINANO).

Declaration of competing interest

All the contributing authors report no conflict of interests in this work.

Author contribution statement

Hongchao Yang and Qiangbin Wang conceived the concept and

Just Accepted

supervised the project. Zhixuan Wang, Zhang Ting, Zhiyong Tang, and Ziyan Zhang synthesized the materials and conducted the structural and optical measurements. Zhixuan Wang, Tingfeng Yao fabricated the devices and collected the performance data of the photodiodes and imaging. Zhixuan Wang, Hongchao Yang, Yejun Zhang, Jiang Jiang and Qiangbin Wang conducted the data analysis. Zhixuan Wang and Hongchao Yang drafted the manuscript. All authors participated in the scientific discussion and revised the manuscript.

Informed consent

Not applicable.

Ethics statement

Not applicable.

Use of AI statement

None.

References

(1) García de Arquer, F. P.; Talapin, D. V.; Klimov, V. I.; Arakawa, Y.; Bayer, M.; Sargent, E. H. Semiconductor Quantum Dots: Technological Progress and Future Challenges. *Science* **2021**, *373* (6555), eaaz8541. https://doi.org/10.1126/science.aaz8541

(2) Park, S. Y.; Paul, S. J.; Li, Z.; Lee, S.; Jo, Y. H.; Hong, E.; Jo, H.; Ahn, Y.; Zheng, H.; Kim, J. H.; Sahu, A.; Kang, M. S. Quad‐Band Short‐Wave Infrared Detection Using Bandgap‐Controlled Ag_2Te Quantum Dots. *Adv Funct Materials* **2025**, e12679. https://doi.org/10.1002/adfm.202512679

(3) Liu, Y.-W.; Ko, D.-K.; Oh, S. J.; Gordon, T. R.; Doan-Nguyen, V.; Paik, T.; Kang, Y.; Ye, X.; Jin, L.; Kagan, C. R.; Murray, C. B. Near-Infrared Absorption of Monodisperse Silver Telluride (Ag_2Te) Nanocrystals and Photoconductive Response of Their Self-Assembled Superlattices. *Chem. Mater.* **2011**, *23* (21), 4657–4659. https://doi.org/10.1021/cm2019795

(4) Mao, C.; Yao, F.; Aleksandrov, D.; Liu, F.; Wu, W. Silver Telluride Quantum Dots on Silicon Near-Infrared Photodetectors. *ACS Appl. Mater. Interfaces* **2025**, *17* (21), 31230–31236. https://doi.org/10.1021/acsami.5c01857

(5) Kim, G.; Choi, D.; Eom, S. Y.; Jung, E. D.; Lee, J. H.; Rehl, B.; Kim, S. Y.; Hoogland, S.; Sargent, E. H.; Jeong, K. S. Extended Short-Wavelength Infrared Ink by Surface-Tuned Silver Telluride Colloidal Quantum Dots and Their Infrared Photodetection. *ACS Mater. Lett.* **2024**, *6* (11), 4988–4996. https://doi.org/10.1021/acsmaterialslett.4c01585

(6) Dai, P.; Wang, Z.; Tang, Z.; Zhang, Z.; Wang, Y.; Yang, X.; Jiang, J.; Zhang, Y.; Yang, H. Bismuth-Doped Ag_2Te Colloidal Quantum Dots for High-Performance Shortwave-Infrared Photodetectors. *Inorg. Chem.* **2025**, *64* (28), 14637–14643. https://doi.org/10.1021/acs.inorgchem.5c02229

(7) Wang, Y.; Peng, L.; Schreier, J.; Bi, Y.; Black, A.; Malla, A.; Goossens, S.; Konstantatos, G. Silver Telluride Colloidal Quantum Dot Infrared Photodetectors and Image Sensors. *Nat. Photonics* **2024**, *18*, 236–242. https://doi.org/10.1038/s41566-023-01345-3

(8) Ahn, Y.; Eom, S. Y.; Kim, G.; Lee, J. H.; Kim, B.; Kim, D.; Si, M.; Yang, M.; Jung, Y.; Kim, B. S.; Chung, Y. J.; Jeong, K. S.; Baek, S. Silver Telluride Colloidal Quantum Dot Solid for Fast Extended Shortwave Infrared Photodetector. *Adv. Sci.* **2024**, *11* (44), 2407453. https://doi.org/10.1002/advs.202407453

(9) Lee, J. A.; Lee, I. S.; Kang, D.; Kim, N.; Kim, J.; Baek, S.-W.; Kim, Y. Chemical Reactivity-Controlled Synthesis of Silver Chalcogenide Colloidal Quantum Dots for Efficient Shortwave Infrared Photodetectors. *Small* **2025**, *21* (20), 2412420. https://doi.org/10.1002/smll.202412420

(10) Wang, Y.; Wu, H.; Rodà, C.; Peng, L.; Taghipour, N.; Dosil, M.; Konstantatos, G. Shortwave Infrared Light Detection and Ranging Using Silver Telluride Quantum Dots. *Adv. Mater.* **2025**, *37* (21), 2500977. https://doi.org/10.1002/adma.202500977

(11) Yuan, D.; Cao, F.; Han, Z.; Liu, M.; Deng, X.; Zhang, L.; Liu, X.; Cao, S.; Liu, X.; Yang, Z.; Deng, Z.; Li, Y.; Voznyy, O.; Fan, Q.; Sun, B.; Huang, W. Zinc Halide Enables Highly Monodisperse Ag_2Te Colloidal Quantum Dots for Short-Wave Infrared Photodetectors. *Nano Energy* **2025**, *140*, 111026. https://doi.org/10.1016/j.nanoen.2025.111026

(12) Konstantatos, G.; Sargent, E. H. Colloidal Quantum Dot Photodetectors. *Infrared. Phys. Technol.* **2011**, *54* (3), 278–282. https://doi.org/10.1016/j.infrared.2010.12.029

(13) Bisri, S. Z. Charge Carrier Injection and Extraction of Colloidal Quantum Dot Assemblies: A Perspective for Optoelectronic Devices. *J. Inf. Disp.* **2025**, *26* (2), 109–130. https://doi.org/10.1080/15980316.2025.2501386

(14) Vokhmintcev, K. V.; Samokhvalov, P. S.; Nabiev, I. Charge Transfer and Separation in Photoexcited Quantum Dot-Based Systems. *Nano Today* **2016**, *11* (2), 189–211. https://doi.org/10.1016/j.nantod.2016.04.005

(15) Clark, S. W.; Harbold, J. M.; Wise, F. W. Resonant Energy Transfer in PbS Quantum Dots. *J. Phys. Chem. C* **2007**, *111* (20), 7302–7305. https://doi.org/10.1021/jp0713561

(16) Zhang, Y.; Wu, G.; Liu, F.; Ding, C.; Zou, Z.; Shen, Q. Photoexcited Carrier Dynamics in Colloidal Quantum Dot Solar Cells: Insights into Individual Quantum Dots, Quantum Dot Solid Films and Devices. *Chem. Soc. Rev.* **2020**, *49* (1), 49–84. https://doi.org/10.1039/C9CS00560A

(17) Oh, S. J.; Straus, D. B.; Zhao, T.; Choi, J.-H.; Lee, S.-W.; Gaulding, E. A.; Murray, C. B.; Kagan, C. R. Engineering the Surface Chemistry of Lead Chalcogenide Nanocrystal Solids to Enhance Carrier Mobility and Lifetime in Optoelectronic Devices. *Chem. Commun.* **2017**, *53* (4), 728–731. https://doi.org/10.1039/C6CC07916D

(18) Yang, Y.; Rodríguez-Córdoba, W.; Lian, T. Multiple Exciton Generation and Dissociation in PbS Quantum Dot-Electron Acceptor Complexes. *Nano Lett.* **2012**, *12* (8), 4235–4241. https://doi.org/10.1021/nl301847r

(19) Zhu, H.; Yang, Y.; Wu, K.; Lian, T. Charge Transfer Dynamics from Photoexcited Semiconductor Quantum Dots. *Annu. Rev. Phys. Chem.* **2016**, *67* (Volume 67, 2016), 259–281. https://doi.org/10.1146/annurev-physchem-040215-112128

(20) Yao, D.; Xin, W.; Liu, Z.; Wang, Z.; Feng, J.; Dong, C.; Liu, Y.; Yang, B.; Zhang, H. Phosphine-Free Synthesis of Metal Chalcogenide Quantum Dots by Directly Dissolving Chalcogen Dioxides in Alkylthiol as the Precursor. *ACS Appl. Mater. Interfaces* **2017**, *9* (11), 9840–9848.

In Accepted

https://doi.org/10.1021/acsami.6b16407

(21) Zhang, M.-Y.; Liu, A.-A.; Fu, H.; Zhang, W.; Zhang, S.-H.; Liu, Z.-Y.; Jiang, L.-H.; Shao, X.; Pang, D.-W. Regulation of Silver Precursor Reactivity via Tertiary Phosphine to Synthesize Near-Infrared Ag_2Te with Photoluminescence Quantum Yield of up to 14.7%. *Chem. Mater.* **2021**, *33* (24), 9524–9533. https://doi.org/10.1021/acs.chemmater.1c02610

(22) Sharma, A.; Yoo, D.; Kim, H.-N.; Choi, M.-J. Sequential Surface Tailoring from Colloid to Solid in Ag_2Te Colloidal Quantum Dots Enables High Hole Mobility and Efficient Shortwave Infrared Photodetection. *Nano Energy* **2025**, *141*, 111091. https://doi.org/10.1016/j.nanoen.2025.111091

(23) Zhou, W.; Zhao, W.; Lu, Z.; Zhu, J.; Fan, S.; Ma, J.; Hng, H. H.; Yan, Q. Preparation and Thermoelectric Properties of Sulfur Doped Ag2Te Nanoparticles via Solvothermal Methods. *Nanoscale* **2012**, *4* (13), 3926. https://doi.org/10.1039/c2nr30469d

(24) Zhang, Y.; Yang, H.; An, X.; Wang, Z.; Yang, X.; Yu, M.; Zhang, R.; Sun, Z.; Wang, Q. Controlled Synthesis of Ag_2Te@Ag_2S Core–Shell Quantum Dots with Enhanced and Tunable Fluorescence in the Second Near‐infrared Window. *Small* **2020**, *16* (14), 2001003. https://doi.org/10.1002/smll.202001003

(25) Wang, Z.; Gu, Y.; Aleksandrov, D.; Liu, F.; He, H.; Wu, W. Engineering Band Gap of Ternary $Ag_2Te_xS_{1-x}$ Quantum Dots for Solution-Processed near-Infrared Photodetectors. *Inorganics* **2023**, *12* (1), 1. https://doi.org/10.3390/inorganics12010001

(26) Chang, Y.; Guo, J.; Tang, Y.-Q.; Zhang, Y.-X.; Feng, J.; Ge, Z.-H. Facile Synthesis of Ag_2 Te Nanowires and Thermoelectric Properties of Ag_2 Te Polycrystals Sintered by Spark Plasma Sintering. *CrystEngComm* **2019**, *21* (11), 1718–1727. https://doi.org/10.1039/C8CE01863D

(27) Tang, Z.; Kotov, N. A.; Giersig, M. Spontaneous Organization of Single CdTe Nanoparticles into Luminescent Nanowires. *Science* **2002**, *297* (5579), 237–240. https://doi.org/10.1126/science.1072086

(28) Yu, M.; Yang, J.; Zhang, X.; Yuan, M.; Zhang, J.; Gao, L.; Tang, J.; Lan, X. In‐synthesis Se‐stabilization Enables Defect and Doping Engineering of HgTe Colloidal Quantum Dots. *Adv. Mater.* **2024**, *36* (27), 2311830. https://doi.org/10.1002/adma.202311830

(29) Lee, W.; Sung, Y.; Kwon, J.; Ha, T.; Lee, G.; Lim, S. J.; Kim, S. Stable versus Labile Ligand Passivation on Silver Chalcogenide Nanocrystals. *ACS Nano* **2026**, *20* (8), 6891–6903. https://doi.org/10.1021/acsnano.5c17559

(30) Tang, Z.; Yang, H.; Sun, Z.; Zhang, Y.; Chen, G.; Wang, Q. The Activity of Zn Precursors Determines the Cation Exchange Reaction Kinetics with Ag_2S: Zn-Doped Ag_2S or Ag_2S@ZnS QDs. *Nano Res.* **2023**, *16* (10), 12315–12322. https://doi.org/10.1007/s12274-023-5952-z

(31) Sarma, D. D.; Nag, A.; Santra, P. K.; Kumar, A.; Sapra, S.; Mahadevan, P. Origin of the Enhanced Photoluminescence from Semiconductor CdSeS Nanocrystals. *J. Phys. Chem. Lett.* **2010**, *1* (14), 2149–2153. https://doi.org/10.1021/jz100698m

(32) Chen, H.; Guo, Y.; Kuznetsova, Y. V.; Sergeeva, K. A.; Portniagin, A. S.; He, X.; Yu, H.; Rogach, A. L.; Zhao, N. Interfacial Engineering with Chemical Bath Deposition for High-Performance HgTe Quantum Dot-Based Short-Wave Infrared Photodetectors. *Nano Convergence* **2025**, *12* (1), 52. https://doi.org/10.1186/s40580-025-00519-9

(33) Kagan, C. R.; Murray, C. B. Charge Transport in Strongly Coupled Quantum Dot Solids. *Nature Nanotech* **2015**, *10* (12), 1013–1026. https://doi.org/10.1038/nnano.2015.247

(34) Maity, P.; Ghosh, H. N. Strategies for Extending Charge Separation in Colloidal Nanostructured Quantum Dot Materials. *Phys. Chem. Chem. Phys.* **2019**, *21* (42), 23283–23300. https://doi.org/10.1039/C9CP03551F

(35) Jiang, Y. Z.; Cui, M. H.; Li, S. S.; Sun, C. J.; Huang, Y. M.; Wei, J. L.; Zhang, L.; Lv, M.; Qin, C. C.; Liu, Y. F.; Yuan, M. J. Reducing the Impact of Auger Recombination in Quasi-2D Perovskite Light-Emitting Diodes. *Nat. Commun.* **2021**, *12* (1), 336. https://doi.org/10.1038/s41467-020-20555-9

(36) Sim, K. M.; Kwon, J.; Ma, J.; Pyo, W. J.; Kim, D.; Sung, Y.; Nam, S. Y.; Joo, T.; Kim, S.; Chung, D. S. Stoichiometric Engineering of Ag_2S Nanocrystals to Realize High Performance for Organic–Inorganic Hybrid Photodiodes. *J. Phys. Chem. C* **2024**, *128* (20), 8540–8548. https://doi.org/10.1021/acs.jpcc.4c02154

(37) Saran, R.; Curry, R. J. Lead Sulphide Nanocrystal Photodetector Technologies. *Nat. Photonics* **2016**, *10* (2), 81–92. https://doi.org/10.1038/nphoton.2015.280

Just Accepted

Electronic Supplementary Material

Ternary Ag-Te-S colloidal quantum dots for shortwave infrared photodetectors

Zhixuan Wang [1,2], Ting Zhang [2], Zhiyong Tang [3], Ziyan Zhang [1,2], Yejun Zhang [2], Jiang Jiang [1,2], Tingfeng Yao [2] ✉, Hongchao Yang [2] ✉, Qiangbin Wang [1,2,3,4] ✉

[1] School of Nano-Tech and Nano-Bionics, University of Science and Technology of China, Hefei 230026, China
[2] CAS Key Laboratory of Nano-Bio Interface, Division of Nanobiomedicine and i-Lab, Suzhou Institute of Nano-Tech and Nano-Bionics, Chinese Academy of Sciences, Suzhou 215123, China
[3] School of Physical Science and Technology, ShanghaiTech University, Shanghai 201210, China
[4] College of Materials Sciences and Opto-Electronic Technology, University of Chinese Academy of Sciences, Beijing 100049, China

Supporting information to https://doi.org/10.26599/NR.2026.94909299

Just Accepted

Address correspondence to Tingfeng Yao, tfyao2022@sinano.ac.cn; Hongchao Yang, hcyang2014@sinano.ac.cn; Qiangbin Wang, qbwang2008@sinano.ac.cn

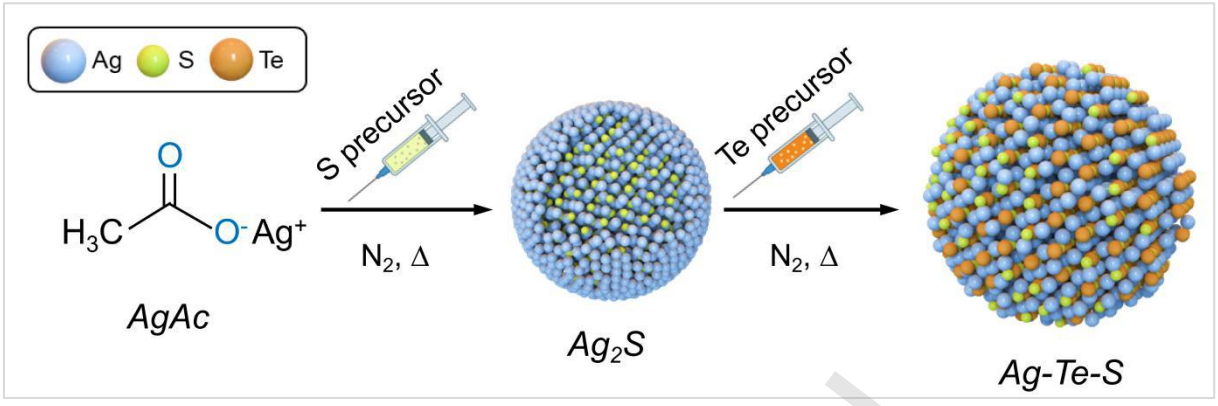

Figure S1. Schematic illustration of the synthetic method of Ag-Te-S QDs.

Just Accepted

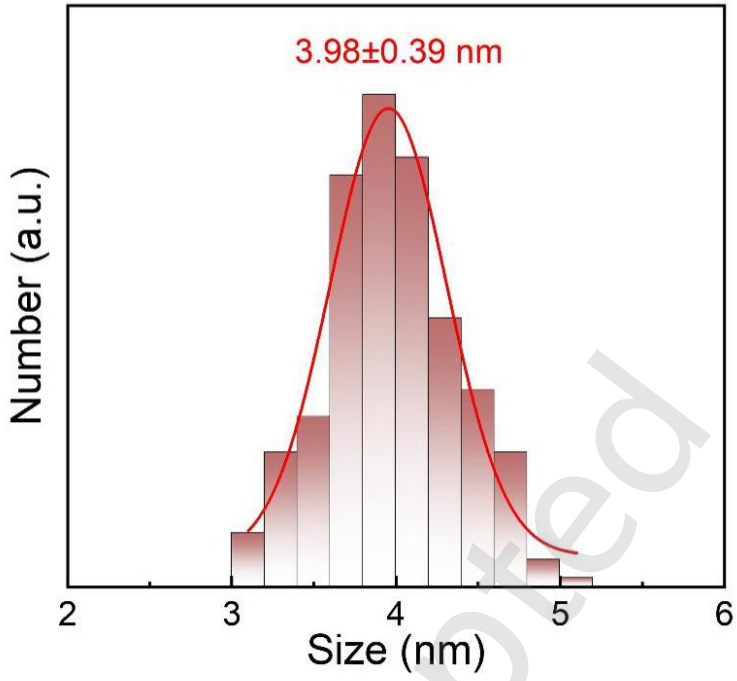

Figure S2. Particle size distribution histograms of Ag-Te-S QDs.

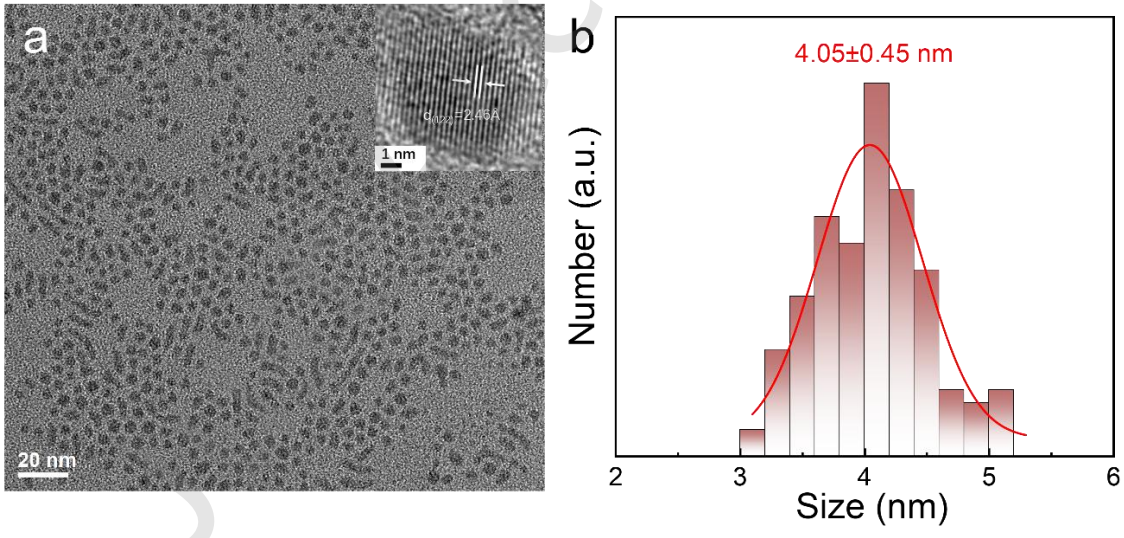

Figure S3. TEM image (a) and particle size distribution (b) of Ag_2Te QDs.

Accepted

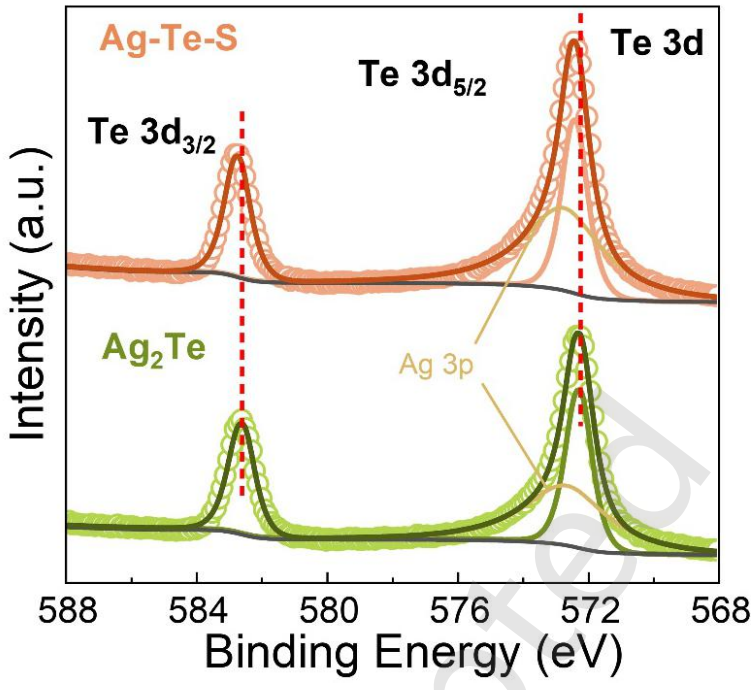

Figure S4. High-resolution XPS spectra of Te 3d of Ag_2Te and Ag-Te-S QDs.

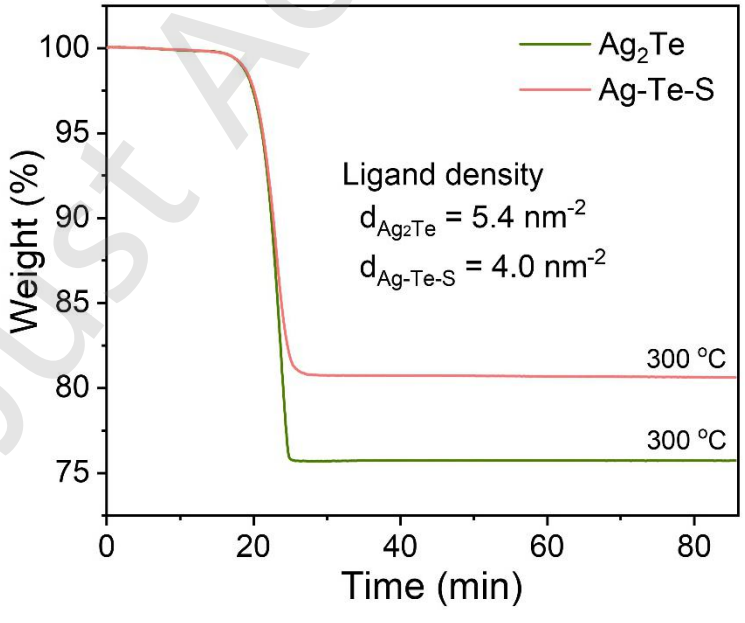

Figure S5. TGA results of Ag_2Te and Ag-Te-S QDs, test temperature: 25-300 °C.

Just Accepted

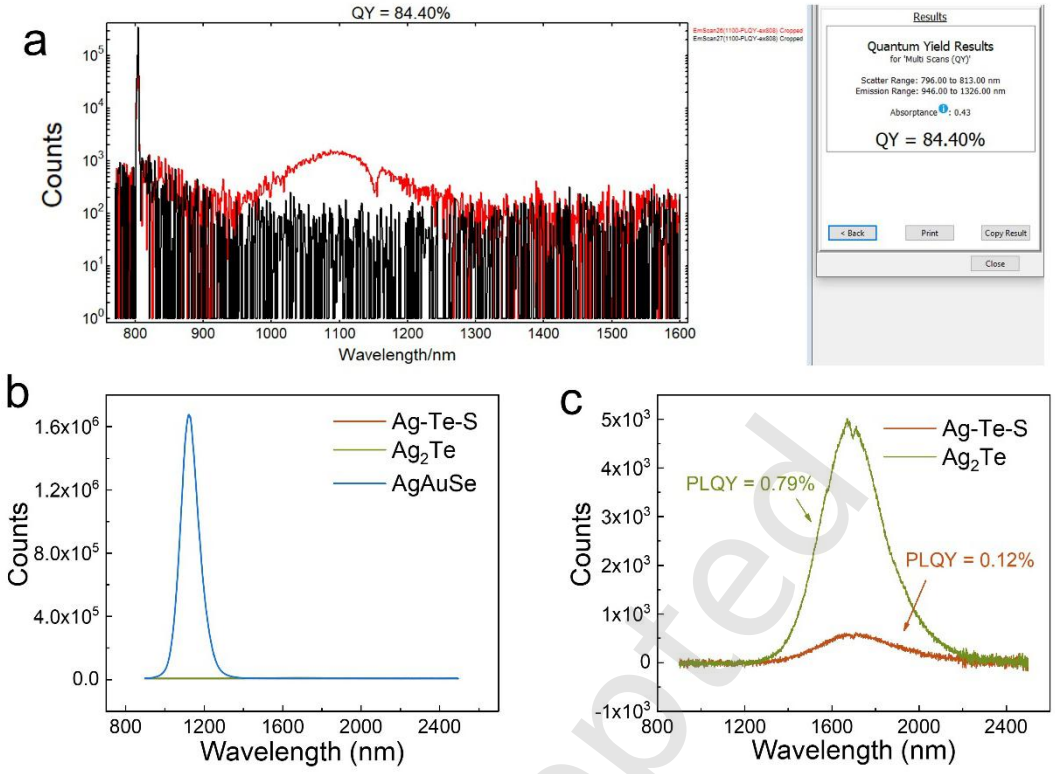

Figure S6. (a) Absolute PLQY of AgAuSe QDs emitted at 1100 nm, which was measured at a calibrated spectrofluorometer (Edinburgh Instruments, FLS1000), laser: 808 nm. (b, c) PL spectra of AgAuSe, Ag_2Te and Ag-Te-S QDs in tetrachloroethylene with the same absorbance at 808 nm, measured under 808 nm laser excitation for PLQY calculation.

Just Accepted

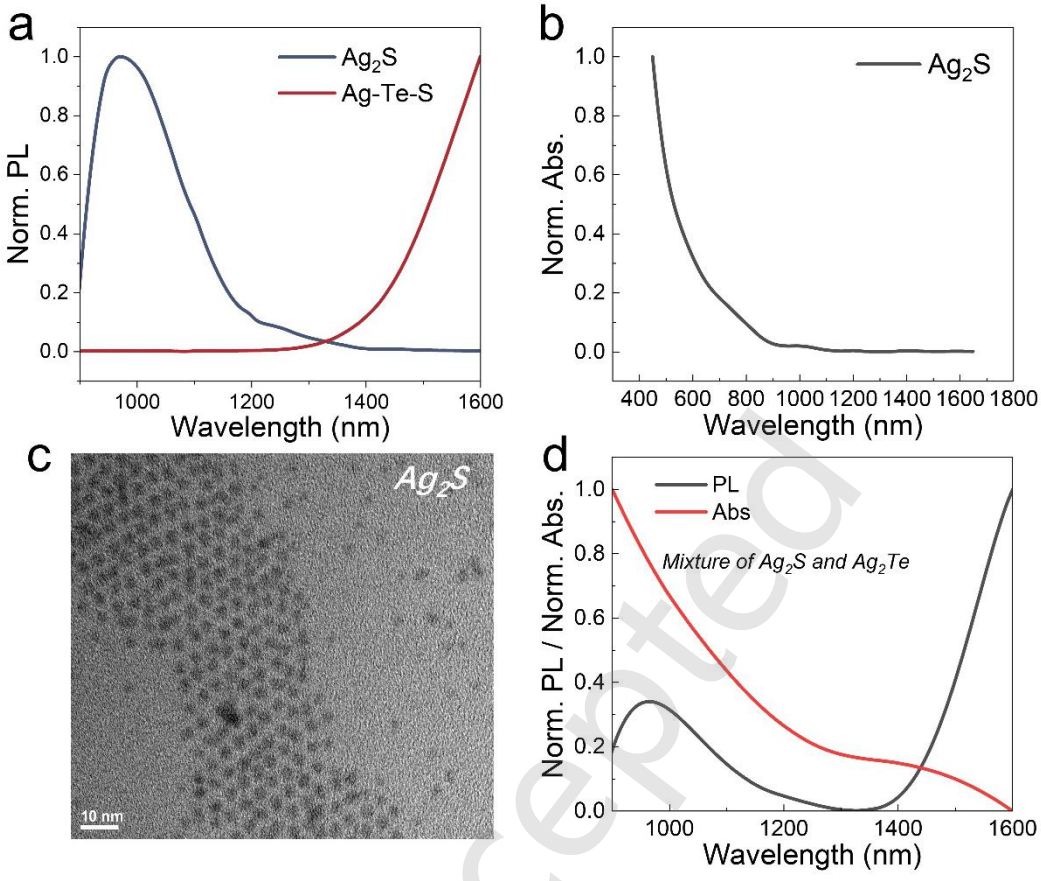

Figure S7. (a) Short-wavelength emission spectra of the Ag-Te-S QDs and the Ag_2S QDs obtained by rapid quenching after sulfur precursor injection. (b) Absorption spectrum of the Ag_2S QDs obtained by rapid quenching after sulfur precursor injection. (c) TEM image of the Ag_2S QDs obtained by rapid quenching. (d) Absorption and emission spectra of the physical mixture of Ag_2S QDs and Ag_2Te QDs with molar ratio 0.27/0.73.

Just Accepted

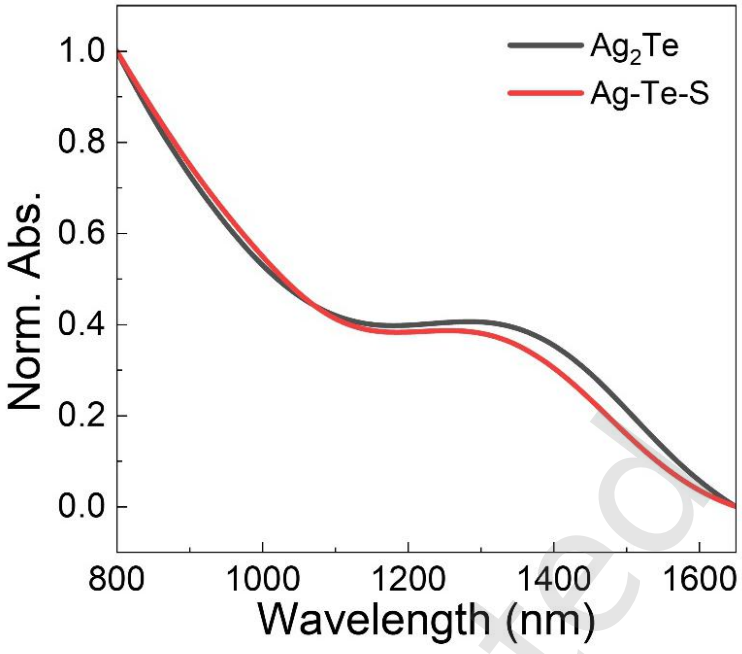

Figure S8. Absorption spectra of the QDs samples used for TAS measurements.

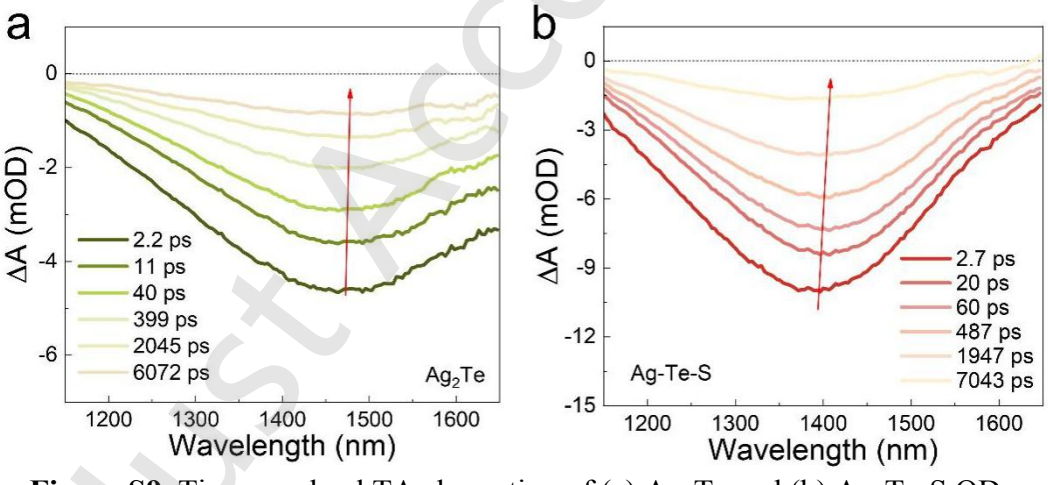

Figure S9. Time-resolved TA absorption of (a) Ag_2Te and (b) Ag-Te-S QDs.

Just Accepted

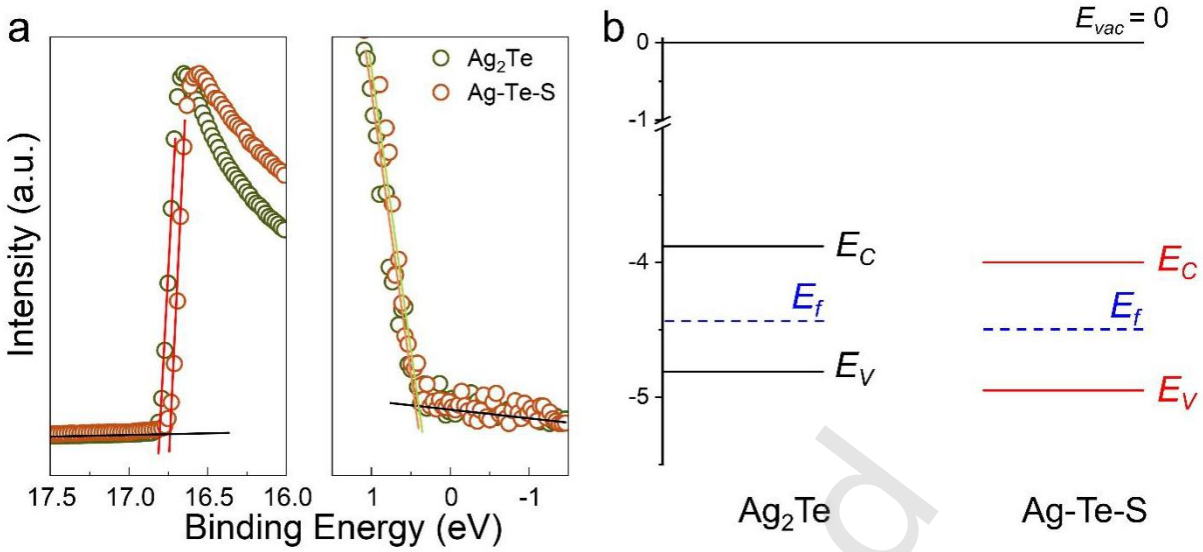

Figure S10. UPS spectra (a) and energy level diagram (b) of Ag_2Te and Ag-Te-S QDs.

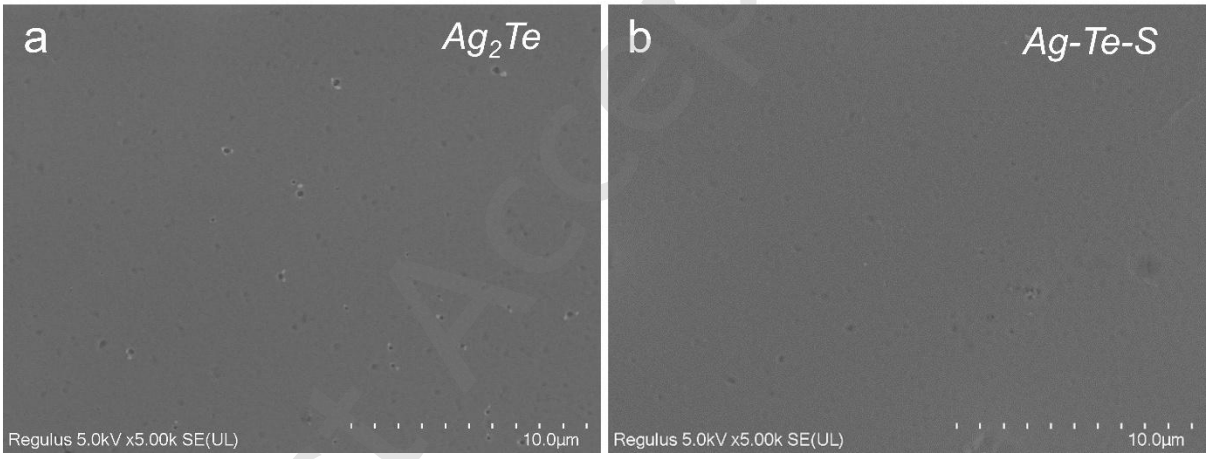

Figure S11. Scanning electron microscopy (SEM) images of Ag_2Te (a) and Ag-Te-S QD (b) films.

Just Accepted

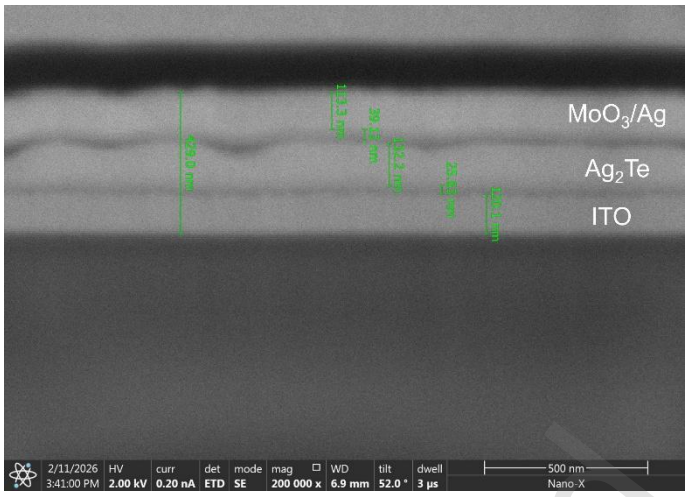

Figure S12. Cross-sectional SEM image of the Ag_2Te QD photodiodes.

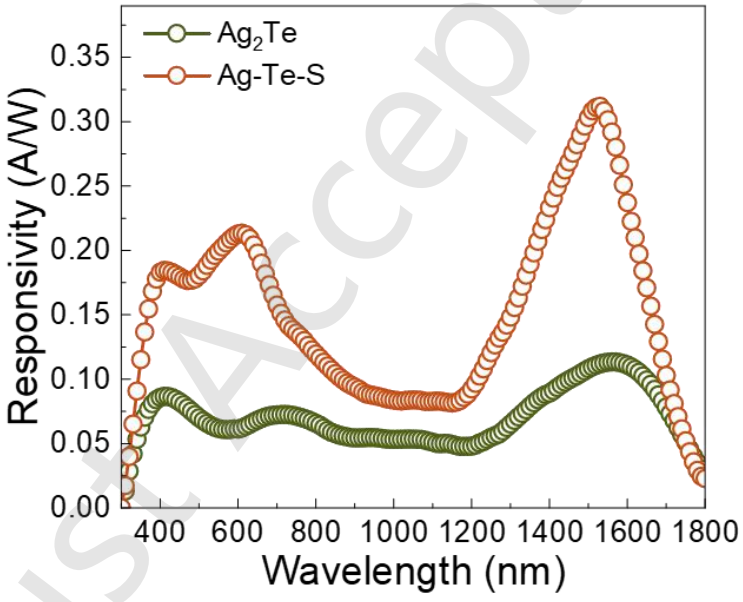

Figure S13. Responsivity of Ag_2Te and Ag-Te-S QD photodiodes.

Just Accepted

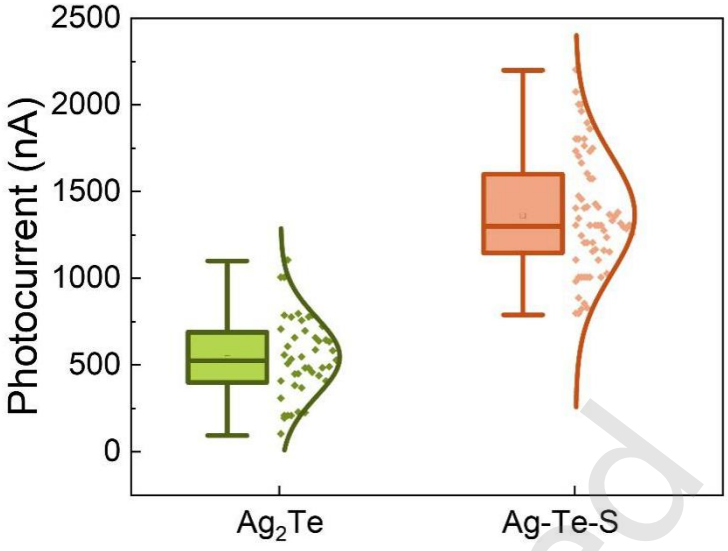

Figure S14. Performance statistics of the net photocurrent at 0 V of Ag_2Te and Ag-Te-S QD devices.

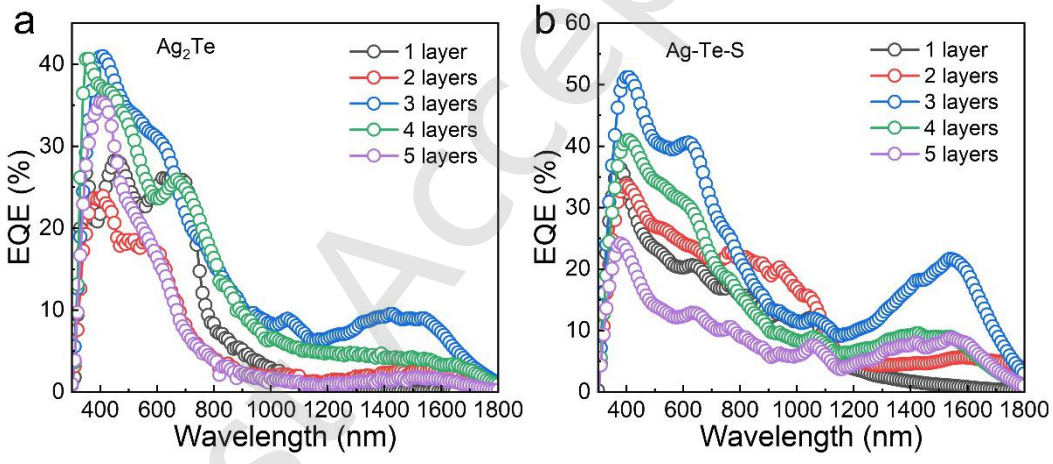

Figure S15. Active-layer-thickness-dependent EQE for Ag_2Te (a) and Ag-Te-S (b) devices.

Just Accepted

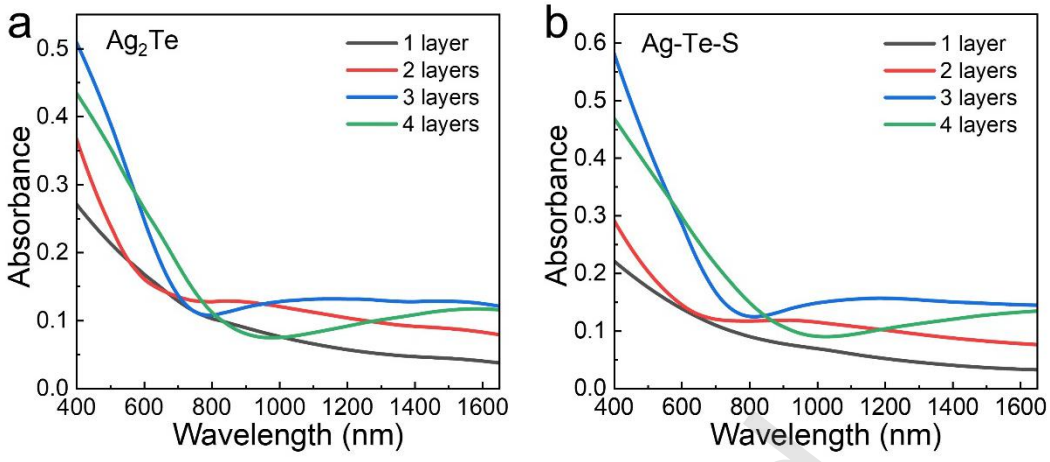

Figure R16. Layer-number-dependent absorption for Ag_2Te (a) and Ag-Te-S (b) devices.

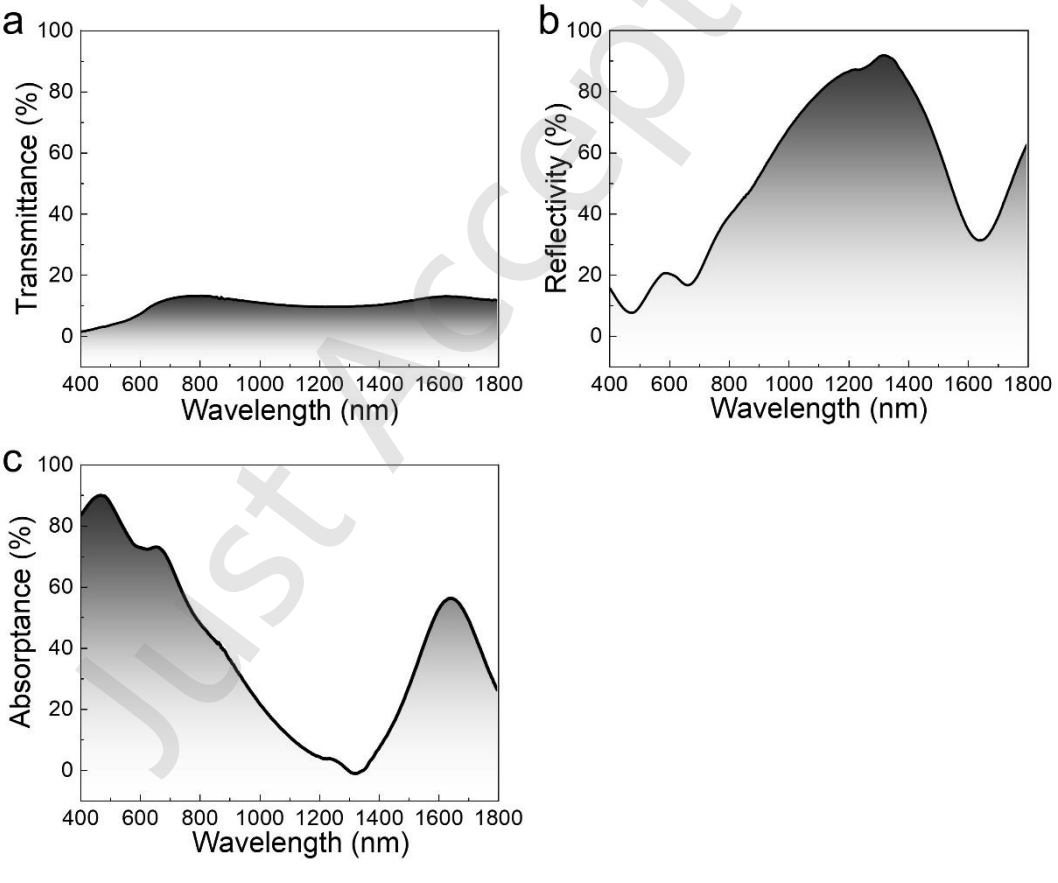

Figure S17. Transmittance (a) and Reflectivity (b) spectra of the completed devices with three-layer Ag-Te-S QD sample. (c) Calculated absorptance spectra of Ag-Te-S devices. According to the Transmittance (T) and Reflectivity (R) data, the absorptance (A) of the devices can be calculated with the following equation: $A = 1-T-R$.

Just Accepted

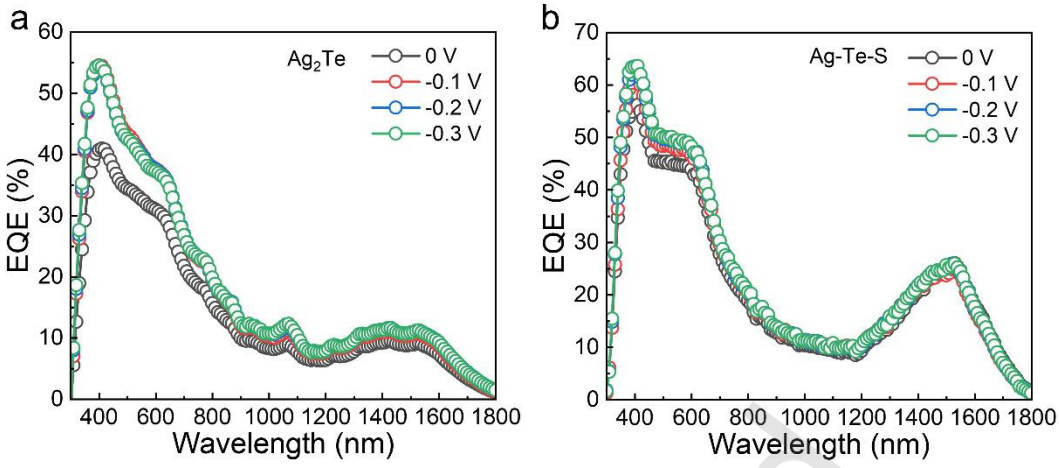

Figure R18. Bias-dependent EQE for Ag_2Te (a) and Ag-Te-S (b) devices.

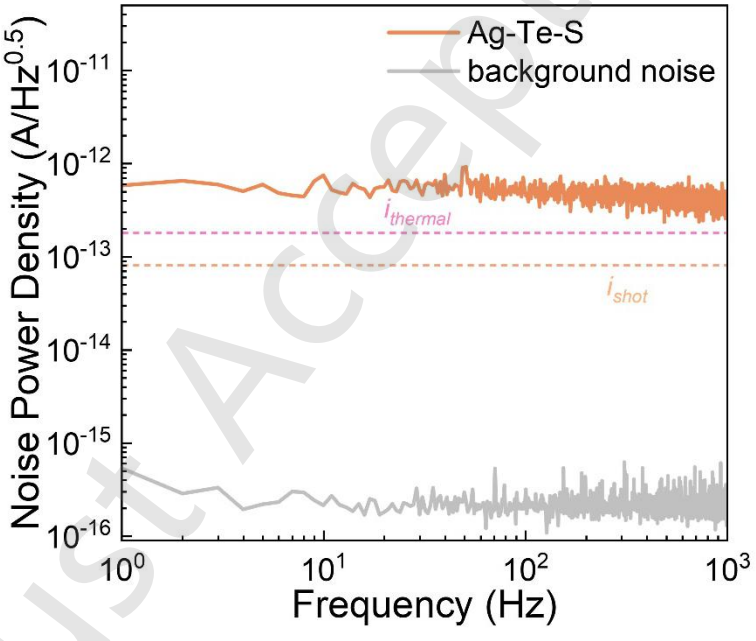

Figure S19. Frequency dependent noise power density. The noise spectral density was measured using a low frequency noise test system (LFN-2000) in RMS average mode with an extremely low noise background of 10^{-16} A/Hz$^{0.5}$.

Just Accepted

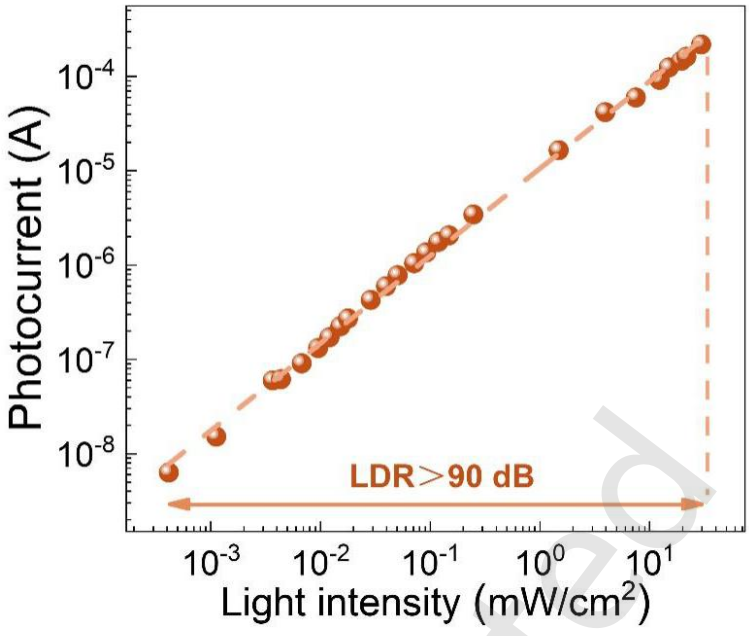

Figure S20. LDR of Ag-Te-S QD photodiode under 1532 nm illumination with power densities from ~1.3 μW cm^{-2} to ~32 mW cm^{-2}.

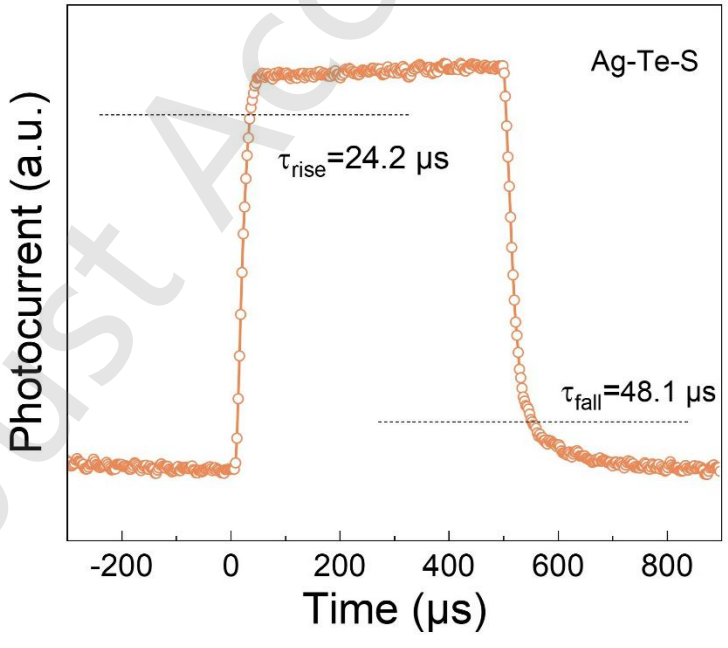

Figure S21. Respond time characterization of Ag-Te-S device at 0 V.

Just Accepted

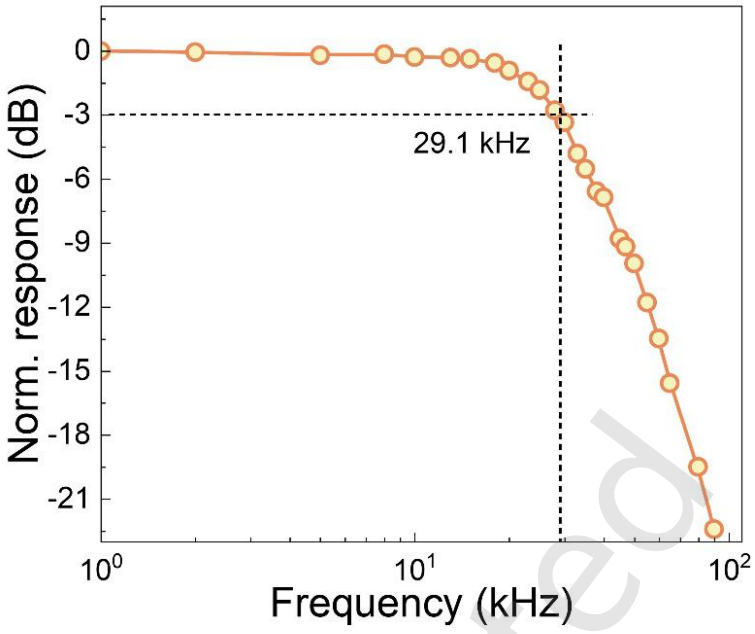

Figure S22. Response bandwidth of Ag-Te-S QD devices.

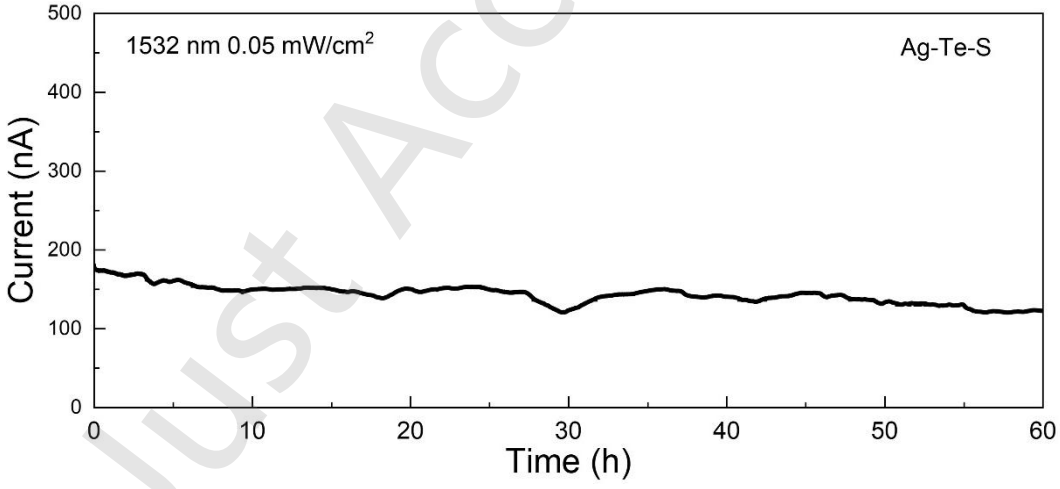

Figure S23. The photoresponse stability of the Ag-Te-S QDs photodiodes measured with under 1532 nm illumination with power densities of 0.05 mW cm^{-2}.

Just Accepted

Table S1. ICP-MS analysis for Ag_2Te and Ag-Te-S QDs

Materials	Ag/ppb	Te/ppb	Ag/Te ratio
Ag_2Te	45.47	25.25	2.08
Ag-Te-S	44.49	18.86	2.75

Table S2. Fitted parameters of the time-resolved PL spectra of Ag_2Te and Ag-Te-S QDs

Materials	τ_1 (ns)	A_1	τ_2 (ns)	A_2	τ_{avg} (ns)
Ag_2Te	3.99	0.48	17.96	0.52	15.57
Ag-Te-S	3.12	0.67	11.88	0.37	9.05

The TRPL was fitted with a bi-exponential function: $I = A_1 \cdot \exp(-\tau/\tau_1) + A_2 \cdot \exp(-\tau/\tau_2) + B$; The average PL lifetimes were calculated by $\tau_{avg}=\sum A_i\tau_i^2/\sum A_i\tau_i$ (i=1, 2).

Table S3. Tri-exponential fitting parameters of the TA dynamics

Materials	τ_1 (ps)	A_1	τ_2 (ps)	A_2	τ_3 (ns)	A_3	τ_{avg} (ns)
Ag_2Te	7.37	-0.39	94.63	-0.23	2.20	-0.30	2.12
Ag-Te-S	18.38	-0.28	172.55	-0.10	3.34	-0.53	3.30

The average carrier lifetimes were calculated by $\tau_{avg}=\sum A_i\tau_i^2/\sum A_i\tau_i$ (i=1, 2, 3).

Table S4. Comparison of V_{TFL} and trap densities extracted using the V_1- and V_2-based SCLC analyses for Ag_2Te and Ag-Te-S QD films

Electron-only	V_1	N_{trap}	V_2	N_{trap}
Ag_2Te	0.12 V	5.31×10^{15}	0.90 V	3.98×10^{16}
Ag-Te-S	0.06 V	2.66×10^{15}	0.44 V	1.95×10^{16}

Hole-only	V_1	N_{trap}	V_2	N_{trap}
Ag_2Te	0.24 V	1.06×10^{16}	0.72 V	3.19×10^{16}
Ag-Te-S	0.24 V	1.06×10^{16}	0.47 V	2.08×10^{16}

Just Accepted

Table S5. Performance statistics of the previously reported QDs SWIR photodetectors

QD Materials	Device area	Dark current	Peak EQE	Response time	D* (Jones)	Ref.
InSb	NA	14 μA/cm^2 @-1 V	33% @1380 nm, 1 V	2.3 μs	1×10^{12} @2 kHz	[1]
InSb	NA	45 μA/cm^2 @-1 V	28% @1450 nm, 1 V	2.5 μs	1.2×10^{10} @10 kHz	[2]
Ag_2Te	3.1 mm^2	2 μA/cm^2 @-0.3 V	20% @1400 nm, 0 V	1.3 μs	10^{10} @1 Hz	[3]
Ag_2Te	1 mm^2	0.4 μA/cm^2 @-0.3 V	20% @1450 nm, 0 V	~600 ns	1.1×10^{11} @1 Hz	[4]
Ag_2Te	NA	40 mA/cm^2 @-0.3 V	16% @1700 nm, 0.3 V	10.6 μs	9.0×10^{10} @10 kHz	[5]
Ag_2Te	10 mm^2	110 μA/cm^2 @-1 V	0.21% @1550 nm, 0 V	0.2 μs	6.1×10^{6} @10 kHz	[6]
Ag_2Te	1 mm^2	60 μA/cm^2 @-0.3 V	2.5% @1550 nm, 0 V	~97 μs	1.4×10^{8} @10 Hz	[7]
Ag_2Te	2.6 mm^2	NA	NA	230 ns	1.2×10^{9} @1 kHz (78 K)	[8]
Ag-Te-S	6 mm^2	9 μA/cm^2 @-0.3 V	26% @1520 nm, 0 V	~24 μs	1.3×10^{11} @1 Hz	*This work*

Table S6. Comparison between Ag-Te-S QD photodetector and commercial InGaAs photodiodes

Photodiodes	λ (nm)	EQE (%)	R (A/W)	D* (Jones)
Ag-Te-S in this work	1520	26%	0.34	1.3×10^{11}
Commercial 1 (InGaAs) Hamamatsu G12181_020K	1550	88%	1.1	1.1×10^{12}
Commercial 2 (InGaAs) Hamamatsu G8370-85	1550	88%	1.1	4.2×10^{12}
Commercial 3 (InGaAs) Hamamatsu G10899-03K	1550	80%	1.0	3.3×10^{12}

Just Accepted

References

[1] M. Imran, D. B. Kim, P. Xia, F. Y. Villanueva, B. Rehl, J. M. Pina, Y. Liu, Y. Zhang, O. Voznyy, E. Kumacheva, S. Hoogland, E. H. Sargent, *Adv. Mater.* **2025**, *37*, 2420273.

[2] Y. Zhang, M. Imran, P. Xia, Y. Chen, A. Gulsaran, Y. Liu, E. Nikbin, B. Rehl, L. Fan, F. Dinic, D. B. Kim, L. Zeng, M. Yavuz, S. Hoogland, E. H. Sargent, *Angew. Chem. Int. Ed.* **2025**, *64*, e202505179.

[3] Y. Wang, L. Peng, J. Schreier, Y. Bi, A. Black, A. Malla, S. Goossens, G. Konstantatos, *Nat. Photonics* **2024**, *18*, 236.

[4] Y. Wang, H. Wu, C. Rodà, L. Peng, N. Taghipour, M. Dosil, G. Konstantatos, *Adv. Mater.* **2025**, *37*, 2500977.

[5] G. Kim, D. Choi, S. Y. Eom, E. D. Jung, J. H. Lee, B. Rehl, S. Y. Kim, S. Hoogland, E. H. Sargent, K. S. Jeong, *ACS Mater. Lett.* **2024**, *6*, 4988.

[6] Y. Ahn, S. Y. Eom, G. Kim, J. H. Lee, B. Kim, D. Kim, M. Si, M. Yang, Y. Jung, B. S. Kim, Y. J. Chung, K. S. Jeong, S. Baek, *Adv. Sci.* **2024**, *11*, 2407453.

[7] D. Yuan, F. Cao, Z. Han, M. Liu, X. Deng, L. Zhang, X. Liu, S. Cao, X. Liu, Z. Yang, Z. Deng, Y. Li, O. Voznyy, Q. Fan, B. Sun, W. Huang, *Nano Energy* **2025**, *140*, 111026.

[8] S. Y. Eom, J. H. Lee, H. Song, S. Son, K. S. Jeong, *Nat. Commun.* **2026**, https://doi.org/10.1038/s41467-026-71374-3.

Just Accepted